e-Proceedings

ICTA2025

International Conference on Traditional and Advanced Ceramics

15-17 October 2025
IMPACT Exhibition & Convention Center, Bangkok, THAILAND

ASEAN Ceramics Thailand
ASEAN Stone Thailand

Organizers

Chula Chulalongkorn University
MTEC a member of NSTDA
The Thai Ceramic Society

Co-Organizers

KU Kasetsart University
KMUTT
School of Science KMITL
The American Ceramic Society Chapter Thailand

Supporters

Upcycle Materials from Industrial and Agricultural Wastes Research Unit Chulalongkorn University
Hub of Talents SustainMat
MRS-Thailand
Messe München
AES

Organizers

Department of Materials Science, Faculty of Science, Chulalongkorn University
National Metal and Materials Technology Center
The Thai Ceramic Society

Co-organizers

Department of Science Service
Faculty of Engineering, King Mongkut's University of Technology Thonburi
Faculty of Engineering, Rajabhat Mahasarakham University
Faculty of Science, Chiang Mai University
Faculty of Science, Prince of Songkla University
Faculty of Science, Ramkhamhaeng University
Faculty of Science and Technology, Nakhon Pathom Rajabhat University
Faculty of Science and Technology, Thammasat University
Institute of Engineering, Suranaree University of Technology
Khon Kaen University
Lampang Rajabhat University
Maejo University
Metallurgy and Materials Science Research Institute, Chulalongkorn University
Rajamangala University of Technology
School of Science, King Mongkut's Institute of Technology Ladkrabang
Srinakharinwirot University
The American Ceramic Society Chapter Thailand

Supporters

Asian Exhibition Services Ltd.
Faculty of Engineering and Industrial Technology, Silpakorn University
Hub of Talent: Sustainable Materials for Circular Economy, PETROMAT, Chulalongkorn University
Institute of Research & Development Phranakhon Rajabhat University
Messe München, MMI Asia Pte. Ltd.
Nakhon Pathom Rajabhat University
The Materials Research Society of Thailand
Upcycle Materials from Industrial and Agricultural Wastes Research Unit, Chulalongkorn Unviersity

Conference Chair

Assoc. Prof. Dr. Sirithan Jiemsirilers, The Thai Ceramics Society and Chulalongkorn University
Assoc. Prof. Dr. Toemsak Srikhirin, National Metal and Materials Technology Center

Technical Chair

Prof. Dr. Nisanart Traiphol, Chulalongkorn University

Technical Committee

Assoc. Prof. Dr. Anantakul Intarapadung, Phranakhon Rajabhat University
Dr. Anucha Wannagon, National Metal and Materials Technology Center
Asst. Prof. Dr. Anurat Poowancum, Suranaree University of Technology
Asst. Prof. Dr. Apirat Theerapapvisetpong, Chulalongkorn University
Assoc. Prof. Dr. Benya Cherdhirunkorn, Thammasat University
Dr. Chalermkwan Makornpan, Ramkhamhaeng University
Asst. Prof. Dr. Chiraporn Auechalitanukul, King Mongkut’s University of Technology Thonburi
Assoc. Prof. Dr. Darunee Vattanasiriweach, Mae Fah Luang University
Assoc. Prof. Dr. Duangrudee Chaysuwan, Kasetsart University
Prof. Dr. Jakrapong Kaewkhao, Nakhon Pathom Rajabhat University
Assoc. Prof. Dr. Jiratchaya Ayawanna, Suranaree University of Technology
Assoc. Prof. Dr. Kamonpan Pengpat, Chiang Mai University
Assoc. Prof. Dr. Kedsarin Pimraksa, Chiang Mai University
Asst. Prof. Dr. Kowit Lertwittayanon, Prince of Songkla University
Dr. Laksana Wangmooklang, Thailand Institute of Scientific and Technological Research
Asst. Prof. Dr. Methee Promsawat, Prince of Songkla University
Asst. Prof. Dr. Mettaya KitiwanKing Mongkut’s Institute of Technology Ladkrabang
Asst. Prof. Dr. Nattaya Tawichai, Mae Fah Luang University
Prof. Dr. Naratip Vitayakorn, King Mongkut’s Institute of Technology Ladkrabang
Asst. Prof. Dr. Nattapol Laorodphan, Maejo University
Asst. Prof. Dr. Neeranut Kuanchertchoo, Ramkhamhaeng University
Dr. Nithiwach Nawaukkaratharnant, Metallurgy and Materials Science Research Institute, Chulalongkorn University
Asst. Prof. Dr. Niti Yongvanich, Silpakorn University
Assoc. Prof. Dr. Nonthaphong Phonphuak, Rajabhat Maha Sarakham University
Dr. Noppakhate Jiraborvornpongsa, Metallurgy and Materials Science Research Institute, Chulalongkorn University
Assoc. Prof. Dr. Nuntaporn Kongkajun, Thammasat University
Assoc. Prof. Dr. Nutthita Chuankrerkkul, Metallurgy and Materials Science Research Institute, Chulalongkorn University

Assoc. Prof. Dr. Oratai Jongprateep, Kasetsart University

Asst. Prof. Dr. Panjasila Payakaniti, Khon Kaen University

Assoc. Prof. Dr. Panpailin Seeharaj, King Mongkut's Institute of Technology Ladkrabang

Asst. Prof. Dr. Pat Soosaen, Silpakorn University

Assoc. Prof. Dr. Patarawagee Yasaka, Nakhon Pathom Rajabhat University

Dr. Pitak Laoratanakul, National Metal and Materials Technology Center

Dr. Phieraya Pulphol, Srinakharinwirot University

Dr. Pranee Junlar, Department of Science Service

Prof. Dr. Prasit Thongbai, Khon Kaen University

Miss Rasnia Tabpla, Department of Science Service

Asst. Prof. Dr. Ryan C. McCuiston, King Mongkut's University of Technology Thonburi

Dr. Saijit Daosukho, Department of Science Service

Dr. Siriporn Larpkiattaworn, Thailand Institute of Scientific and Technological Research

Asst. Prof. Dr. Sittinun Tawkaew, Srinakharinwirot University

Assoc. Prof. Dr. Siwat Lawanwadeekul, Lampang Rajabhat University

Dr. Sorachon Yoriya, National Metal and Materials Technology Center

Asst. Prof. Dr. Suthee Wattanasiriwech, Mae Fah Luang University

Dr. Sutthima Sriprasertsuk, Department of Science Service

Assoc. Prof. Dr. Thanakorn Wasanapiarnpong, Chulalongkorn University

Assoc. Prof. Thitima Khunyotying, Lampang Rajabhat University

Asst. Prof. Dr. Thitirat Charoonsuk, Srinakharinwirot University

Asst. Prof. Dr. Worapong Thiemsorn, Chiang Mai University

Asst. Prof. Dr. Yongyut Khamkhong, Phranakhon Rajabhat University

Table of Contents

Effect of Propylene Glycol Content on Rheology, Cure Depth, and Debinding Behavior of Alumina Suspensions for LCD 3D Printing

Worachet Supasorn [a, *], Thanakorn Wasanapiarnpong [a,b]
[a] Upcycled Materials from Industrial and Agricultural Wastes Research Unit, Department of Materials Science, Faculty of Science, Chulalongkorn University, Phyathai Road, Bangkok, 10330, Thailand
[b] Center of Excellence on Petrochemical and Materials Technology, Chulalongkorn University, Bangkok, 10330, Thailand
*Corresponding author e-mail address: 6570155323@student.chula.ac.th

Abstract

Liquid Crystal Display (LCD) 3D printing is a vat photopolymerization technique that employs an LCD screen and an LED light to selectively cure a liquid photopolymer resin layer by layer. Owing to its high resolution and cost-effectiveness, LCD printing has become widely adopted in dentistry for fabricating dental models and appliances. Achieving an optimal balance between ceramic particle content and suspension viscosity remains a key challenge in ceramic 3D printing. This study presents the fabrication of alumina (Al_2O_3) ceramics with LCD 3D printing, with propylene glycol (PPG) employed as a non-reactive diluent to tailor the rheological properties of the ceramic suspension. Alumina powder with an average particle size of 0.4 µm and a solid loading of 30 vol% was combined with varying PPG concentrations (10, 20, and 30 vol%) to investigate their effects on suspension stability and printability. In addition, the green and sintered bodies were prepared for flexural strength and Vickers hardness testing. However, severe cracking after sintering prevented reliable mechanical data acquisition. Resin solution properties were analyzed by Viscometer (Brookfield DV-E) and Cure depth testing. Low-temperature thermal debinding was performed on the printed samples. Higher PPG concentrations reduced interlayer cracking during the early debinding stage, but excessive PPG (30 vol%) led to severe cracking and fragmentation after sintering. These results highlight the trade-off between improved flowability during printing and increased cracking risk during high-temperature processing.

Keywords: LCD 3D printing; alumina ceramics; propylene glycol (PPG); rheology; cure depth

Background

Additive manufacturing (AM) of ceramics has gained significant attention in recent years due to its capability to fabricate complex geometries that are difficult to achieve through conventional forming methods. Among the various AM techniques, vat photopolymerization (VPP) offers excellent dimensional precision and surface quality for ceramic components. It includes stereolithography (SLA), digital light processing (DLP), and liquid crystal display (LCD) printing. In this process, liquid photosensitive resin containing fine ceramic particles is cured layer by layer under ultraviolet or visible light to form a solid object directly from a computer-designed model.

Achieving a homogeneous, printable ceramic suspension remains a major challenge in vat photopolymerization (VPP) of ceramics. Ceramic powders have high refractive indices, which tend to increase viscosity and interrupt flowability, especially at high solid loadings. Although a high particle concentration is desirable to ensure good mechanical strength after sintering, it often causes light scattering and poor layering during printing. These rheological and optical limitations can lead to insufficient curing or weak interlayer bonding in printed parts. Therefore, optimizing the rheology of the suspension and light penetration for polymerization are important for achieving a stable layer, uniform curing, and high-quality ceramic components in LCD-based 3D printing.

Alumina (Al_2O_3) is one of the most commonly used oxide ceramics in additive manufacturing because of its high hardness, wear resistance, and chemical stability. However, its relatively high refractive index (~1.76) causes strong scattering of the curing light, limiting polymerization depth and making the process more sensitive to formulation design. Recent studies have explored the use of dispersants, coupling agents, and non-reactive diluents to improve printability [1-3].

Among the various diluents, propylene glycol (PPG) is of particular interest because it effectively lowers viscosity and improves flowability without participating in the cross-linking reaction. However, excessive addition of PPG can dilute reactive monomers, reduce light penetration, and weaken interlayer adhesion. To achieve the appropriate balance, it is important to understand how different PPG concentrations affect both rheology and polymerization behavior in alumina suspensions.

In this study, the influence of PPG content on the viscosity, cure depth, and printability of alumina-based photopolymer resins for LCD 3D printing is investigated. The results provide insights into optimizing resin formulations that balance good flowability and curing performance, thereby improving process stability and structural integrity in ceramic 3D printing.

Materials and Methods

Sample preparation

High-purity alumina (Al_2O_3) powder with an average particle size of 0.4 µm was used as the ceramic phase. The solid loading was fixed at 30 vol% in all suspensions. The photosensitive resin consisted of trimethylolpropane triacrylate (TMPTA) as the reactive monomer, with propylene glycol (PPG) as a non-reactive diluent to adjust viscosity and enhance flowability.

A silane coupling agent (KH-560, 1 wt%) was added to improve interfacial bonding between the alumina surface and the polymer matrix. BYK-111 (0.5 %wt) was used as a dispersant, and TPO (2,4,6-trimethylbenzoyl-diphenylphosphine oxide, 3 %wt) served as the photoinitiator.

Table 1 Composition of alumina suspensions for LCD 3D printing

Batch	TMPTA (vol%)	PPG (vol%)	Alumina (vol%)
B1	40	30	30
B2	50	20	30
B3	60	10	30
B4	70	0	30

All ingredients were weighed according to **Table 1** and mixed in a planetary ball mill at 300 rpm for 2 h using zirconia jars and balls. The suspensions were degassed under vacuum for 15 min to remove air bubbles before printing.

Printing was performed using an LCD-based 3D printer (Phrozen Sonic Mini 8K) equipped with a 405 nm light source. The layer thickness was set to 50 µm, and the exposure time was optimized according to the cure-depth results. After printing, the green parts were rinsed with isopropyl alcohol (IPA) to remove uncured resin and dried at room temperature.

Water debinding

Water debinding was carried out by immersing samples in deionized (DI) water for 24 h to remove PPG and other soluble organics.

Sintering

After drying, specimens were sintered in air using a high-temperature furnace. The heating schedule was as follows: the furnace temperature was increased from 30 °C to 200 °C at 1 $°C\cdot min^{-1}$, then to 600 °C at 1 $°C\cdot min^{-1}$, then to 1600 °C at 3 $°C\cdot min^{-1}$ hold 2 h, and furnace-cool to room temperature.

Characterization

Slurry characterizations

The viscosity of each suspension was measured at 25 °C using a Brookfield DV-E viscometer (spindle No. 4, 100 rpm).

The cure depth was evaluated using the Beer–Lambert working-curve model. Thin layers (~0.5 mm) were exposed to 405 nm UV for 15, 30, 45, and 60 s. Cured thickness (C_d) was measured with a digital micrometer and fitted with Equation (1):

$$C_d = D_p \ln\left(\frac{E_0}{E_c}\right) \qquad (1)$$

Where D_p is the penetration depth (mm), E_0 is the exposure energy ($mJ\cdot cm^{-2}$), and E_c is the critical energy.

Mechanical characterizations

The linear shrinkage (δ) was determined by vernier caliper measurements before and after sintering:

$$\delta = \frac{L_0 - L}{L_0} \times 100\% \qquad (2)$$

where L_0 and L are green body and sintered lengths, respectively [3].

The Deformation (D) was calculated by Equation (3):

$$D = \frac{2H_{center} - H_{left} \quad _{right}}{2H_{center}} \times 100\% \qquad (3)$$

where H_{center} is the height measured at the specimen center and H_{left} and H_{right} are the heights measured at the left and right edges, respectively.

The flexural strength (σ) of debound and sintered bars was measured by a three-point bending test (Instron 5882). Strength was calculated by:

$$\sigma = \frac{3PL}{2bh^2} \qquad (4)$$

where P is the maximum load (N), L is the span (mm), b is the width (mm), and h is the thickness (mm).

The hardness of a material was analyzed using a Vickers hardness tester, which determines hardness by the size of an indentation created under a specified load by a pyramid-shaped diamond indenter. The Vickers number (HV) is calculated using the following formula.

$$\mathrm{HV} = 1.854\frac{P}{d^2} \text{..................} (5)$$

With P being the applied load (kgf) and d is the average diagonal length of the indentation (mm). The applied load is usually specified when HV is cited.

Results and Discussion

Rheological behavior of alumina suspensions

The viscosity of the alumina suspensions was strongly influenced by the amount of propylene glycol (PPG) added. The base formulation without PPG (B4) exhibited the highest viscosity, approximately 1535 cP, which limited particle movement and resulted in poor flowability during printing.

When PPG was incorporated, the viscosity decreased markedly to about 270 cP for the 30 vol% formulation (B1). The presence of PPG improved the suspension's flow behavior by reducing internal resistance within the resin matrix. Similar trends have been reported in other ceramic-filled systems, where non-reactive diluents enhance fluidity and facilitate layer formation during printing [2,4].

However, excessive PPG (30 vol%) can weaken the resin network and reduce crosslinking efficiency, resulting in poor structural strength of the printed green body. Therefore, a moderate PPG content of 10-20 vol% (B2–B3) offers a balanced combination of low viscosity and stable dispersion, which is critical for achieving uniform light exposure and minimizing surface defects in LCD-based 3D printing.

As illustrated in **Figure 1**, the viscosity of the suspensions decreased sharply with increasing PPG concentration, confirming that the addition of PPG effectively improves the flowability of the alumina slurry.

Cure-depth analysis

The relationship between cure depth and exposure time followed the Beer–Lambert working-curve model (Equation 1). The experimental results, shown in **Figure 2**, indicate that the cure depth increased with longer exposure time for all formulations, but the increase became smaller as the PPG content rose [3,5].

Suspensions containing higher PPG concentrations exhibited shallower curing depths, mainly due to reduced light transmission and lower polymerization efficiency. When PPG was added, the higher dilution of reactive monomers and slight light scattering within the slurry limited the depth to which light could effectively cure the resin.

The penetration depth (D_p) decreased from approximately 0.20 mm for B4 to 0.13 mm for B1, while the critical exposure energy (E_c) increased from 4.8 to 7.6 mJ·cm⁻². These results suggest that PPG influences the suspension's optical properties, requiring higher energy to achieve the same curing depth.

From a processing perspective, insufficient penetration depth (<0.12 mm) may result in weak layer adhesion, whereas excessive depth (>0.22 mm) can lead to overcuring and reduced z-resolution. Among all formulations, B2 (20 vol% PPG) achieved the most balanced curing behavior, providing stable interlayer bonding and accurate dimensional control during LCD printing.

The working curves clearly demonstrate the logarithmic relationship between exposure time and cure depth, confirming that the Beer–Lambert model accurately describes the curing behavior of the alumina suspensions.

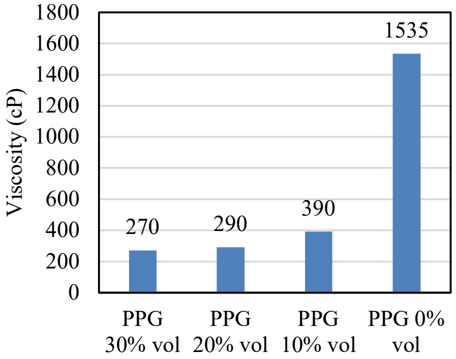

Figure 1 Viscosity of alumina suspensions with different PPG contents.

Shrinkage and deformation after debinding

The measured linear shrinkage along the x-, y-, and z- axes for different PPG concentrations is illustrated in **Figure 3**. The shrinkage values increased slightly with higher PPG content, ranging from approximately 1–6%, depending on the printing direction. The formulation containing 30 vol% PPG exhibited the highest overall shrinkage, particularly in the z-axis (≈6%), while the formulation without PPG (0%) showed the lowest values (<2%).

This behavior indicates that greater amounts of PPG introduce more organic material that must be removed during water debinding and drying, leading to larger volumetric changes. The higher z-direction shrinkage also reflects the build-up of residual stress along the printing direction, where layer interfaces are most affected by polymer removal.

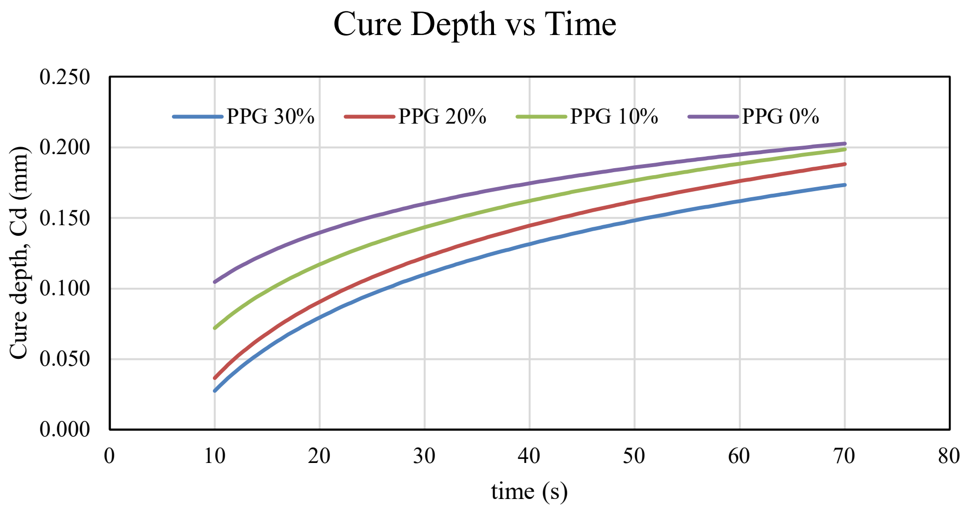

Figure 2 Working curves of alumina suspensions with different PPG contents.

The deformation trends are shown in **Figure 4**. The warpage percentage was highest for samples with 10–30 vol% PPG, reaching up to 4.5%, while the 20 vol% PPG formulation showed the lowest deformation (~2%). The slight concave curvature observed in the high-PPG samples can be attributed to differential drying rates and internal stress gradients within the green body.

These results confirm that moderate PPG addition (20 vol%) provides a good balance between reduced viscosity for printability and sufficient rigidity to maintain structural stability. Excessive or insufficient PPG content both lead to greater deformation due to uneven drying and internal stress concentration [2,6].

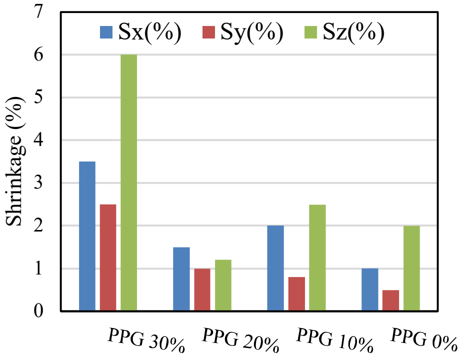

Figure 3 Linear shrinkage comparison of alumina suspensions with different PPG contents.

Shrinkage after sintering

The linear shrinkage of the alumina samples after sintering is shown in **Figure 5**. All samples exhibited shrinkage between 21-28%, which is typical for alumina ceramics fabricated by vat photopolymerization. The shrinkage values were consistent among the x-, y-, and z-directions, confirming that the sintering process was uniform and well-controlled.

For the B2 (20 vol% PPG) and B3 (10 vol% PPG) formulations, the shrinkage values were around 24–26%, indicating stable particle packing and uniform densification. The formulation without PPG (B4) showed slightly lower shrinkage of about 21–22%, which may be due to limited particle rearrangement caused by its higher viscosity during printing.

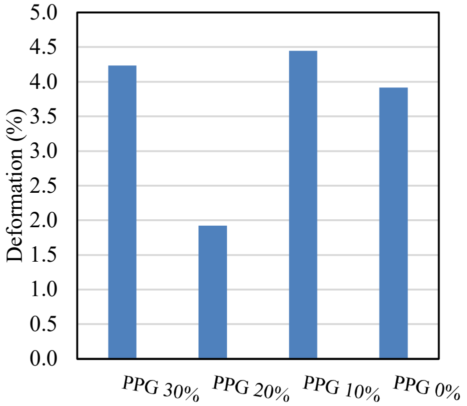

Figure 4 Deformation percentage of alumina suspensions after water debinding.

In contrast, the B1 (30 vol% PPG) specimens could not be measured due to severe cracking and fragmentation after sintering, as shown in **Figure 6**. The excessive organic content in this formulation likely resulted in high internal gas pressure and uneven shrinkage during debinding, leading to catastrophic failure. It is expected that the B1 composition would have exhibited higher shrinkage (around 26–28%) due to the larger void volume created during binder removal.

Overall, moderate PPG addition (10–20 vol%) produced the most balanced sintering behavior, combining low deformation, controlled shrinkage, and consistent densification across all directions. This suggests that resin formulations with an optimized PPG ratio can effectively minimize warpage while maintaining uniform shrinkage during high-temperature sintering [1,7].

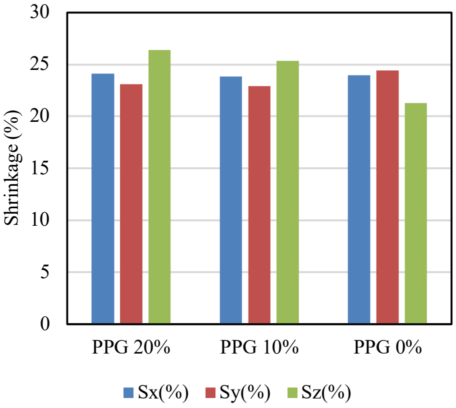

Figure 5 Linear shrinkage of alumina suspensions with different PPG contents after sintering.

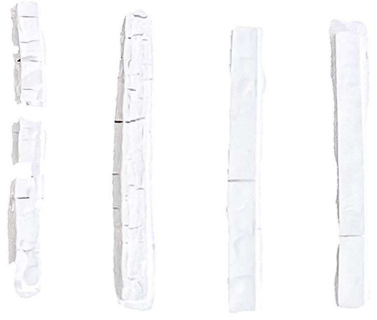

B1 PPG 30 vol% **B2 PPG 20 vol%** **B3 PPG 10 vol%** **B4 PPG 0 vol%**

Figure 6 Fractured alumina specimens after sintering showing severe cracking in the 30 vol% PPG formulation after sintering.

Sintering behavior and fractured observation

After sintering, all specimens exhibited varying degrees of visible cracking, as shown in Figure 6. The cracks were primarily oriented along the printing direction and extended through the cross-section, indicating high internal stress during debinding and sintering. Although the overall geometry of the bars was preserved, none of the samples remained fully intact, making precise linear shrinkage measurement impossible.

The 30 vol% PPG (B1) specimens displayed the most severe fragmentation, breaking into multiple segments. This failure can be attributed to the excessive organic content, which produced high internal gas pressure and stress gradients during binder burnout. The soft green body, formed by the high PPG level, lacked sufficient strength to resist shrinkage-induced stress, leading to delamination and layer separation.

The 20 vol% (B2) and 10 vol% (B3) formulations also developed longitudinal cracks, but to a lesser extent. Their partial densification suggests that moderate PPG improved the homogeneity of the printed layers; however, the internal stress generated during drying and debinding remained sufficient to cause crack formation at the weak interlayer boundaries.

The 0% PPG (B4) sample exhibited fewer cracks but remained brittle, with a rougher surface texture, likely due to poor particle packing and limited densification caused by the high resin viscosity.

Overall, these results reveal that cracking occurred across all compositions, though it was most pronounced in the high-PPG formulation (B1).

Future work will focus on optimizing the debinding and sintering profiles—particularly by applying slower heating ramps (0.3–0.5 °C·min^{-1} between 200–380 °C) and using powder-bed or BN-coated setters—to reduce thermal stress and achieve crack-free sintered alumina components

Mechanical properties

Mechanical testing could not be performed for most sintered specimens due to cracking and incomplete densification. The samples with 30 vol% PPG (B1) fractured severely during the sintering process, while minor surface cracks were also observed in the 0% PPG (B4) formulation. Because of these defects, neither flexural strength nor Vickers hardness could be accurately measured.

The failure to obtain mechanical data is primarily due to the high internal stress generated during binder removal and sintering. The large organic fraction in the B1 formulation likely caused excessive gas evolution and uneven shrinkage, leading to structural weakness and premature cracking. In contrast, the formulations with 10–20 vol% PPG (B2–B3) showed intact geometry and are expected to exhibit higher mechanical strength due to improved layer bonding and uniform densification.

Further work will focus on optimizing the debinding and sintering profiles to prevent cracking and enable accurate mechanical characterization in future tests.

Conclusion

This study investigated the influence of propylene glycol (PPG) content on rheological behavior, curing performance, and dimensional stability of alumina suspensions for LCD-based 3D printing. The results demonstrated that PPG plays a crucial role in controlling both the printability and the structural integrity of the printed ceramic parts.

Increasing the PPG content effectively reduced the resin viscosity, thereby enhancing flowability and layer uniformity during printing. Nevertheless, excessive addition (30 vol%) led to a reduced curing depth, poor interlayer adhesion, and severe cracking after sintering, primarily due to the high organic content and non-uniform shrinkage. Moderate PPG contents of 10–20 vol% provided the most balanced performance, combining low viscosity, sufficient curing depth, and reduced deformation, although cracking during sintering still prevented complete densification and mechanical testing.

Although mechanical testing was not possible due to sample cracking, structural observations indicate that optimized PPG ratios can significantly improve the reliability and dimensional accuracy of LCD-printed alumina ceramics. Future work will focus on refining the debinding and sintering profiles to eliminate cracking and to evaluate the mechanical properties of the optimized compositions.

Overall, this research provides fundamental insights into how non-reactive diluents affect the processing–structure relationship in photopolymerizable ceramic systems, offering practical guidance for designing printable and defect-free alumina formulations for high-precision additive manufacturing applications.

Acknowledgements

We would like to thank the lab members and the Department of Materials Science, Faculty of Science, Chulalongkorn University, for their support and assistance.

References

1. J. Kim, C.W. Gal, Y.-J. Choi, H. Park, S.-Y. Yoon, H.-S. Yun, Effect of non-reactive diluent on defect-free debinding process of 3D printed ceramics, *Addit. Manuf.*, 67, 103475 (2023).
2. X. Li, S. Feng, C. Song, W. Wang, Strategic design and functional evaluation of oligomer components in vat photopolymerization 3D printing of alumina ceramics, *J. Eur. Ceram. Soc.*, 45, 117676 (2025).
3. H. Chen, L. Wang, Z. Zhang, Fabrication of porous aluminum ceramics beyond device resolution via stereolithography 3D printing, *Ceram. Int.*, 49, 18463–18469 (2023).
4. X. Li, Y. Zhao, Y. Liu, Optimization of acrylate oligomer ratios for improved rheology and photopolymerization in ceramic suspensions, *Ceram. Int.*, 51, 24680–24692 (2025).
5. H. Chen, L. Wang, Y. Zhang, Cure-depth characteristics and working-curve analysis of alumina-loaded photopolymer resin, *Ceram. Int.*, 49, 14210–14221 (2023).
6. Z. Li, P. Wang, Q. Huang, Effect of PEGDA and TMPTA ratio on curing kinetics and shrinkage of ceramic photopolymer resin, *J. Eur. Ceram. Soc.*, 44, 2381–2391 (2024).
7. J. Kim, D.-S. Kim, H.-S. Yun, Effect of dispersants on structural integrity of 3D printed ceramics, *Int. J. Appl. Ceram. Technol.*, 19, 968–978 (2022).

Synthesis of Hydroxyapatite Powders by Chemical Precipitation with Substitution of Transition Metal Ions for Solar Reflective Pigments

Thanakorn Wasanapiarnpong[1,2,3]*, **Pimpagee Pancharat**[1] , **Uraiwan Leela-adisorn**[1] **and Charusporn Mongkolkachit**[4]
[1] Department of Materials Science, Faculty of Science, Chulalongkorn University, Phyathai Road, Pathumwan, Bangkok 10330, Thailand
[2] Center of Excellence on Petrochemical and Materials Technology, Chulalongkorn University Research Building, Phayathai Road, Pathumwan, Bangkok 10330, Thailand
[3] Upcycled Materials from Industrial and Agricultural Wastes Research Unit, Department of Materials Science, Faculty of Science, Chulalongkorn University, Phyathai Road, Bangkok, 10330, Thailand
[4] National Metal and Materials Technology Center, National Science and Technology Development Agency, Khlong Luang, Pathumthani 12120, Thailand
*Corresponding author e-mail address: thanakorn.w@chula.ac.th

Abstract

Hydroxyapatite ($Ca_{10}(PO_4)_6(OH)_2$) is an inorganic compound composed of hydrated calcium phosphate, which has garnered interest due to its ease of synthesis, environmental friendliness, resistance to weathering, and its light-reflecting properties, particularly in the near-infrared (NIR) wavelength range corresponding to solar heat radiation. This research aims to explore its potential application as a solar-reflective pigment. Hydroxyapatite was synthesized via an aqueous chemical precipitation method using calcium hydroxide and phosphoric acid, with 10 mol% partial substitution of calcium ion site by transition metal ions incorporated into the hydroxyapatite crystal structure. Water soluble sulfate and chloride compounds of chromium, copper, iron, and nickel were used for comparison. The resulting modified hydroxyapatite powders exhibited different colors, including white, purple, blue-green, blue, orange, and light yellow, respectively. The results showed that chloride precursors led to pure hydroxyapatite phase, while sulfate precursors resulted in the presence of gypsum as a secondary phase. The pigments doped with chromium and iron exhibited high NIR reflectance values of up to 83.38% and 82.87%, respectively. Additionally, the synthesized pigments were found to have high fineness with particle sizes below 200 nanometers.

Keywords: Hydroxyapatite, Solar Reflective Pigment, Transition Metal Substitution, NIR reflectance

Background

Precipitation is a simple and low-temperature synthesis method that can yield large quantities of product while utilizing water as the reaction medium. However, impurities may sometimes be introduced because ions from the solution can be incorporated into the final structure. To obtain highly pure precipitated products, a higher precipitation temperature in combination with an increased solution pH typically above 4.2 is recommended to minimize structural contamination. In addition, the precipitation method often results in hydroxyapatite particles with low crystallinity and compositions that deviate from stoichiometric ratios [1, 2]. Hayek and Stadlman proposed a precipitation reaction to avoid contamination originating from coprecipitation, as shown in Equation (1):

$$10Ca(OH)_2 + 6H_3PO_4 \rightarrow Ca_{10}(PO_4)_6(OH)_2 + 18H_2O \quad \text{(equation 1)}$$

S. Lazić and colleagues investigated the effect of reaction temperature on the precipitation synthesis of hydroxyapatite using a calcium hydroxide suspension prepared from calcium oxide and deionized water. This suspension was reacted with phosphoric acid and subjected to thermal treatment at 22 °C - 95 °C for 20 hours. Their results indicated that hydroxyapatite synthesized at 95 °C exhibited the highest thermal stability [3].

Hydroxyapatite is widely used as a biomedical material, such as in dental prostheses, bone implants, and drug delivery systems. Recently, increasing attention has been given to modifying the hydroxyapatite structure to improve its optical properties in both the visible and invisible regions. Wenjing Tang and co-workers[4] studied apatite-structured pigments doped with transition metals. The materials synthesized via solid-state reaction at 600-1350 °C had the general formula $A_5(MO_4)_3X$, where M = Fe, Mn, or Cu, yielding yellow-orange, blue, and reddish-purple pigments, respectively. X-ray diffraction analysis revealed that Mn- and Cu-doped samples produced a single-phase hexagonal hydroxyapatite without secondary phases, whereas Fe-doped samples exhibited the α-$Ca_3(PO_4)_2$ phase, with its abundance increasing at higher Fe contents. UV/Vis reflectance measurements (200–2500 nm) showed that undoped hydroxyapatite exhibited reflectance above 95% in the near-infrared (NIR) region, whereas doping with Fe, Mn, or Cu decreased NIR reflectance. In this study, hydroxyapatite is denoted as HAp, and the dopants Fe, Mn, and Cu are represented as F, M, and C, respectively, followed by numbers indicating doping concentrations.

Komalakrushna Hadagalli et al. [5] examined Fe^{3+} substitution in hydroxyapatite using $FeCl_3$ (0.01-0.05 M). The doped materials had the formula $Ca_{10-x}Fe_x(PO_4)_6(OH)_2$, and the pigment color became darker with increasing Fe content. Higher Fe^{3+} incorporation enhanced absorption in the 200–400 nm and 300-700 nm regions, with maximum absorption at 240 nm. Lattice contraction was observed due to Fe^{3+} substituting Ca^{2+} sites, leading to calcium-deficient hydroxyapatite (CD-HA) and a reduced Ca/P ratio.

Near-infrared radiation is the major component of solar energy reaching Earth's surface, accounting for nearly 52% of total solar radiation, with wavelengths ranging from 700 to 2500 nm-beyond the range visible to the human eye. Heat accumulation in objects on the Earth's surface is primarily caused by absorption of NIR radiation [6].

Pigments capable of reflecting NIR radiation have become increasingly important. Complex inorganic color pigments (CICPs), which are synthesized from two or more metal oxides with mineral-like structures, are of particular interest due to their excellent thermal and chemical stability, resistance to acids and solvents, and long-term color durability under UV exposure. In addition to visible-light coloration, CICPs can reflect NIR wavelengths, thereby reducing heat transfer and heat buildup in coated surfaces. This makes them suitable for exterior architectural coatings and other cooling applications.

Given these considerations, the present work focuses on the use of hydroxyapatite (HAp, $Ca_5(PO_4)_6OH_2$) as a white pigment and its structural modification using transition metals. Hydroxyapatite is an attractive host lattice due to its ability to accommodate cation substitution-such as transition metal ions replacing Ca^{2+} sites-while maintaining the overall apatite structure. The synthesized samples are investigated for their optical properties in both the visible and NIR regions (700-2500 nm) to assess their suitability as heat-reflective pigments, particularly since NIR radiation accounts for approximately 52% of solar energy and significantly contributes to heat accumulation on surfaces [4, 7]. The precipitation method is selected for synthesis because it is simple, produces large quantities of material, requires no high-temperature processing, and is environmentally friendly [8].

Materials and Methods

A. Raw materials and methods

The samples were prepared from H_3PO_4 with a concentration of 85% W/W, $Ca(OH)_2$ powder, transition metals with a 10 mol% ($Ca_9M(PO_4)_6(OH)_2$ where M is the transition metal) i.e., $CoSO_4 \cdot 7H_2O$, $Fe_2(SO_4)_3 \cdot xH_2O$, $NiSO_4 \cdot 6H_2O$ and $CrSO_4 \cdot 5H_2O$ were used as sulfate compounds addition. Moreover, $CoCl_2 \cdot 6H_2O$, $FeCl_3 \cdot 6H_2O$, $NiCl_2 \cdot 6H_2O$, $CrCl_3 \cdot 6H_2O$ were also used as chloride compounds addition. Initially, a $Ca(OH)_2$ suspension was prepared by mixing $Ca(OH)_2$ powder and DI water with magnetic stirring. Then, H_3PO_4 was mixed with transition metal and DI water using magnetic stirring for the metal solution. The metal solution was slowly added to the $Ca(OH)_2$ suspension and stirred for 1 hour, resulting in the precipitation of modifying HAp. The resulting slurry was then sealed by plastic film over the beaker's edge and heated to 80 °C for 24 hours. Later, the plastic film was unsealed, and the mixture was dried at 100 °C for 24 hours. The powder samples were accessed after the powder was ground in a mortar and sieved with a 100-mesh sieve, the powder samples were accessed. All the sample were marked as HAp, FeS, CrS, CoS and NiS, as pure HAp, modified HAp, with the sulfate compounds of Fe, Cr, Co and Ni, respectively.

B. Characterization techniques

The crystal phase was analyzed by X-ray diffraction (XRD). The data were collected in the 2θ range of 5°-80° with a step size of 0.02°. Also, using XRD to analyze cell volume (Å^3) and lattice parameters. The samples' colors resulted using The Commission Internationale de l'Eclairage (CIE*)* system (L*, a* and b*) with the colorimeter, where L* indicates from black (0) to white (100), a* represents red (+a*) -green (-a*) axis, b* prefers blue (-b*) -yellow (b*) axis.

The UV-Vis-NIR reflectance spectra of the samples were recorded with a UV-vis-NIR spectrophotometer (Agilent Cary 7000) in the wavelength range of 250-2500 nm using poly-tetrafluoroethylene (PTFE) as a reference standard. The sample's solar energy reflectance (Rs) in a range of NIR (700-2500 nm) was calculated using ASTM standard number G159-98.(Standard, 1998) Below is the listed formula:

$$R_s = \frac{\int_{700}^{2500} \mathrm{R}(\lambda) E_\lambda d\lambda}{\int_{700}^{2500} E_\lambda d\lambda}$$

R_s represents the sample's solar reflectance, λ stands for wavelength, R(λ) indicates the material's spectral reflectance at that specific wavelength, and E_λ refers to the solar spectral irradiance.

Results and Discussion

A. Chromatic properties

The photographs of synthesized powders in the natural light state were shown in Figure 1. The pure HAp was white in appearance. While Fe was substituted in HAp powder, they turned orange. The color of the Co doped powder was pale purple. When Cr entered HAp simultaneously, turning cyan. The powder got a yellow hue when Ni ion took place in the HAp structure. Varied types of dopant ions were manipulated to produce a range of vibrant color pigments.

According to the colorimetric data, the color coordinates values of pigments were shown in Table 1. The lightness (L*), redness (a*), and yellowness (b*) values varied based on the samples' composition. The pure HAp had the highest L* (94.03). No matter whether it was doped with any transition ion, the L* value decreased. Generally, the -a* value could be observed in the modified HAp with Cr and Ni ions, which confirmed samples in green hue. The Co had b* negative (-4), and Cr's b* value was close to zero (1.19); the pigment had a blue shade. While Fe had a* and b* positive values, the sample was nearly red-yellow, which resulted orange in color.

B. X-ray diffraction analysis

The XRD patterns of HAp with Fe, Cr, Co, and Ni were illustrated in Figure 2. It showed that all the samples presented characteristic diffraction peaks of hydroxyapatite with a space group of (JCPDS 01-084-1998). The HAp, Co, and Ni had pure hydroxyapatite phase with no other impurity phase, while in the case of Fe and Cr, gypsum phase (JCPDS 01-070-0982) was observed at approximately 14.81° and 29.82°. All the samples' main phase of HAp was shifted to the smaller 2-theta, which confirmed that the transition ions and fluoride ion substituted in the HAp structure.

C. Reflectance spectra NIR

The samples' solar reflectance (250-2500 nm) spectra were shown in Figure 3, and the calculated NIR (700-2500 nm) reflectance was reported. As the modifying transition metal, the solar reflectance (R_s)

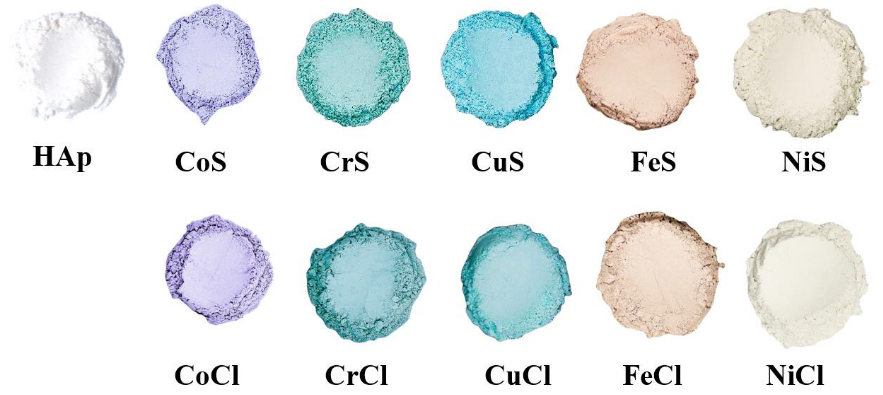

Figure 1 Synthesized powders of pure HAp, modified HAp with Fe, Cr, Co and Ni in the natural light.

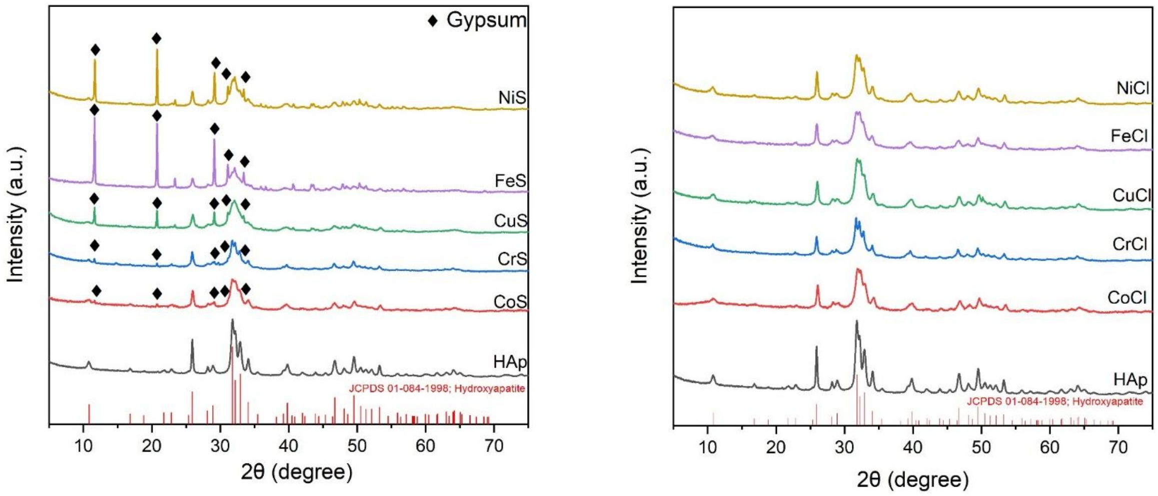

Figure 2 Comparison of XRD patterns of all samples.

decreased. As expected in the case of modified HAp with Cr, the near-infrared reflectance was increased from 77.04% to 83.38%. The NIR reflectance of modified HAp with Fe was 82.87%. For modifying Co ion, the Rs decreased to 54.08%. While Cu had the lowest NIR reflectance, at 32.01%. Even though the NIR reflectance of doped HAps was lower than that of pure HAps, they still had NIR reflective properties.

Table 1 The color coordinates data of samples.

Samples	**Color coordinates**		
	L*	a*	b*
HAp	94.03	0.64	2.76
CoS	74.15	4.43	-0.55
CoCl	71.58	3.85	-1.09
CrS	79.48	-9.36	-0.58
CrCl	78.58	-10.26	-0.03
CuS	87.19	-12.35	-7.48
CuCl	89.91	-9.79	-3.35
FeS	85.33	3.68	19.62
FeCl	87.32	1.86	15.83
NiS	92.82	-4.19	9.54
NiCl	91.46	-2.54	11.38

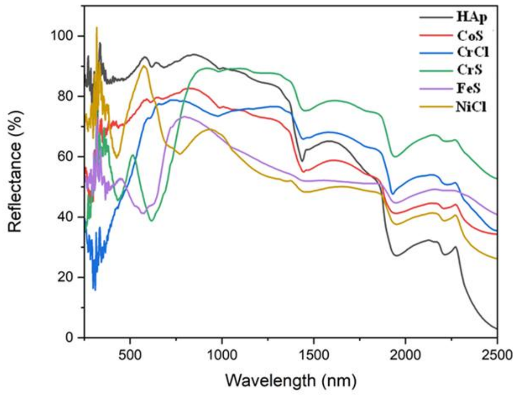

Figure 3 Diffuse reflectance spectra of the samples (250-2500 nm).

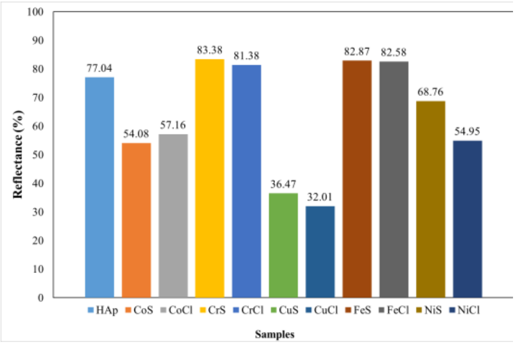

Figure 4 The calculated NIR (700-2500 nm) reflectance of samples.

Conclusion

In this study, the effects of transition-metal ion modification on the optical properties of hydroxyapatite were investigated. Hydroxyapatite was synthesized via a precipitation method using calcium hydroxide and phosphoric acid at 80 °C for 24 h. For the transition-metal chlorides, the filtrate was discarded and the turbid suspensions were washed thoroughly with deionized water prior to drying at 100 °C. Filtration through Whatman No. 42 paper was performed until the supernatant became colorless to prevent the formation of $CaCl_2$ phases in the system.

Phase analysis revealed that all synthesized samples exhibited hydroxyapatite as the primary phase, while gypsum was additionally detected in samples modified with transition-metal sulfates. X-ray diffraction patterns showed decreased crystallinity upon transition-metal incorporation, as evidenced by the broadening and merging of the three main hydroxyapatite peaks-indicating increasing structural disorder. This suggests that the incorporation of various dopant ions induced lattice distortion within the hydroxyapatite framework.

The optical characterization showed distinct color changes when hydroxyapatite was modified with cobalt, chromium, copper, iron, and nickel ions, producing purple, bluish-green, blue, orange, and pale yellow pigments, respectively. Regarding near-infrared reflectance, samples modified with chromium sulfate, chromium chloride, iron sulfate, and iron chloride exhibited reflectance values of 83.38%, 81.30%, 82.87%, and 82.58%, respectively, demonstrating that metal-ion modification influenced the NIR-reflective properties of hydroxyapatite.

References

[1] Elisa Fiume, Giulia Magnaterra, Abbas Rahdar, Enrica Verné, Francesco Baino, **Hydroxyapatite for biomedical applications: A short overview**, *Ceramics*, Vol. 4 [4], pp. 542-563 (2021).

[2] Muhammad Usman Munir, Sajal Salman, Ayehsa Ihsan, Tilal Elsaman, **Synthesis,**

characterization, functionalization and bio-applications of hydroxyapatite nanomaterials: an overview, *International journal of nanomedicine*, Vol., pp. 1903-1925 (2022).

[3] Slavica Lazić, Slavica Zec, Nada Miljević, Slobodan Milonjić, **The effect of temperature on the properties of hydroxyapatite precipitated from calcium hydroxide and phosphoric acid**, *Thermochimica acta*, Vol. 374 [1], pp. 13-22 (2001).

[4] Wenjing Tang, Wei Xu, Mingfeng Zhong, Zhijie Zhang, **Slightly doped hydroxyapatite pigments of subtractive color with high near-infrared reflectance**, *Journal of Solid State Chemistry*, Vol. 322, pp. 123947 (2023).

[5] Komalakrushna Hadagalli, Sulakshana Shenoy, Kaushal R Shakya, Kartick Tarafder, Saumen Mandal, Bikramjit Basu, **Effect of Fe3+ substitution on the structural modification and band structure modulated UV absorption of hydroxyapatite**, *International Journal of Applied Ceramic Technology*, Vol. 18 [2], pp. 332-344 (2021).

[6] Vinod C Malshe, Ashwini K Bendiganavale, **Infrared reflective inorganic pigments**, *Recent Patents on Chemical Engineering*, Vol. 1 [1], pp. 67-79 (2008).

[7] Sheethu Jose, Deepak Joshy, Soumya B Narendranath, Pradeepan Periyat, **Recent advances in infrared reflective inorganic pigments**, *Solar Energy Materials and Solar Cells*, Vol. 194, pp. 7-27 (2019).

[8] NAS Mohd Pu'ad, P Koshy, HZ Abdullah, MI Idris, TC Lee, **Syntheses of hydroxyapatite from natural sources**, *Heliyon*, Vol. 5 [5], pp. (2019).

Copper Oxide - Cobalt Oxide Composite Fibers for Catalyzing a Nitrate Reduction Reaction

Chiraporn Auechalitanukul [1*], Ryan McCuiston [1], Jakkapat Jeephet [1], Natthawat Phochanapun [1], Woradorn Phromphon [1]
[1] Department of Tool and Materials Engineering, Faculty of Engineering, King Mongkut's University of Technology Thonburi, Bangkok, 10140, Thailand
*Corresponding author e-mail address: chiraporn.aue@kmutt.ac.th

---

Abstract

Copper oxide - cobalt oxide composite fibers were synthesized and their performance as catalysts for the reduction of nitrate to ammonia was evaluated. Ammonia is a vital chemical for the agricultural and industrial sectors and holds significant potential as an energy source. The synthesis of ammonia via nitrate reduction requires less energy and emits less carbon dioxide compared to the conventional Haber-Bosch process. In this study, electrospinning was used to fabricate Cu/Co containing fibers, followed by calcination at 400, 500, 600, and 700°C to create oxides. The effect of calcination temperature on the fiber characteristics was studied using XRD and SEM. The catalytic performance of the fibers was assessed using chronoamperometry and UV-Vis spectroscopy. Copper containing fibers were electrospun using a mixture of polyacrylonitrile and copper acetate. The fibers were then treated with a hexacyanocobaltate solution to add cobalt. The calcined fibers were found to contain a mixture of copper oxides (CuO and Cu_2O) and cobalt oxides (CoO and Co_3O_4), the amount depending on the calcination temperature. The fibers calcined at 600°C achieved the highest Faradaic efficiency and had an ammonia yield enhancement 18 times greater compared to a bimetallic electrodeposited catalyst, based on catalyst mass. It is suggested this was a result of the high surface area of the fibers. Although fibers calcined at 400 and 500°C also had high surface areas, the amount of cobalt oxide they contained was too low to aid catalytic activity. At 700°C, the surface area decreased due to pore blockage, which reduced the catalytic performance. The development of mixed-oxide fibers may contribute to nitrate reduction in wastewater, pollution mitigation, and ammonia production, with potential applications in wastewater treatment systems and small-scale ammonia production in areas lacking infrastructure.

Keywords: Electrocatalyst; Electrospinning; Fibers; Nitrate Reduction; Oxide Catalyst.

Background

As a result of overuse or runoff of chemicals, water resources can become polluted, which is obviously undesirable, as water is very vital to living creatures, and humans are no exception. **Eutrophication,** a form of pollution, is the acceleration of algae growth that results from **high levels of nitrogen** in the water. One of the causes of this is the overuse of fertilizers in agricultural activity. Nitrate (NO_3^-) in the water, often used in fertilizers, is a nitrogen compound that can be reduced by a reduction reaction, the so called **"nitrate reduction reaction" (NtRR)**. By NtRR, ammonia can be produced, a chemical that is widely used in the chemical industry and is a potent medium for energy storage. The use of NtRR can reduce the amount of nitrate in water while producing ammonia for other uses.

In NtRR, **deoxygenation** and **hydrogenation** are the main reactions used to convert nitrate to ammonia. Via an electrochemical reaction, a catalyst can be used to prevent the unwanted byproducts of NtRR. The use of metallic catalysts for NtRR, such as copper, nickel, platinum, and palladium, have been widely studied, however, non-metallic catalysts are also feasible and have also been studied. Bimetallic catalysts, such as copper-nickel, and copper-cobalt [1], are likely to catalyze each reaction involved in NtRR. While precious metals are effective catalysts, they are very expensive [2]. The advantage of using transition metals is a relatively low cost and durability [3] but the drawback is unwanted byproducts [4]. The bimetallic catalysts have been found to reduce the activation energy and unwanted byproducts of NtRR [5, 6]. The metal oxides, such as NiO, Co_3O_4, MnO_2, were reported to be more stable catalysts for NtRR, as they assisted the electron transfer required for nitrate production [7, 8].

In this manuscript, the potential use of a non-metallic catalyst is shown, with two oxide catalysts; copper oxide and cobalt oxide, used to accelerate the reactions. In addition, a high number of catalyst active sites is desired to increase the reaction rates. While coating of a metal catalyst directly on the surface of a substrate by electroplating is common, a catalyst formed on a fiber substrate, or a catalyst fiber itself, could offer more surface area for NtRR. Nanofibers of phosphorized CuCo/C for sensing glucose have been successfully prepared by electrospinning [9]. In this study, electrospinning was used to fabricate fibers which were then heated to various temperatures to study the effects on the characteristics of catalyst fibers and on the electrochemical reaction product yield rate (i.e. ammonia yield rate).

Materials and Methods

Oxide fiber preparation

Electrospinning was used to fabricate fibers containing copper and cobalt, with the process involving several steps. The electrospinning procedure followed the method of Cao *et al.* [9]. Copper and cobalt were incorporated into fibers though a process of electrospinning and soaking. The first step was to prepare a polyacrylonitrile–copper(II) acetate (PAN–$Cu(Ac)_2$) solution, the second step was to electrospin the prepared solution into fibers, the third step was to incorporate cobalt into the fibers by soaking them in Potassium hexacyano-cobaltate: ($K_3[Co(CN)_6]$ at 45°C for 24 hours, and the fourth step, the fibers were dried and calcined at different temperature (400, 500, 600, and 700°C) to obtain oxide fibers. The calcination was performed in a loosely-sealed glass-tube furnace with a heating rate of 2°C per minute and with a nitrogen gas flow of 18 ml per minute, to remove decomposition products, and heated to the designed temperature for one hour, before cooling.

Characterization of fibers

Phase analysis of the calcined fibers was studied via an X-ray diffractometer (XRD) (model: D8 Discover, Bruker, USA). The shape of the calcined fibers was observed using a scanning electron microscope (SEM) (model: Nova NanoSEM 450, FEI, USA). The specific surface area of the calcined fibers was analyzed using the BET method.

Electrochemical experiment

The electrochemical characterization used in this study was adopted from Wu *et al.* [1]. In the electrochemical setup, three electrodes: a working electrode (calcined fiber deposited carbon electrode), a reference electrode (Hg/HgO) and a counter electrode (Pt electrode), were used to study the NtRR. An electrolyte solution containing 1 M KOH and 0.1 M KNO_3 was used. Using a potentiostat (1287A Electrochemical interface, Solartron Analytical, UK), the chronoamperometry was performed for 15 minutes. Then the electrolyte solution was collected for ammonium chloride concentration measurement. By mixing with an indophenol blue solution, the mixed solution was then analyzed by UV-VIS spectrometer (model: Spectrophotometer U-3900, Hitachi, Japan). In this study, the absorption at 636 nm (wavelength) was used to create a standard curve of absorption and ammonium chloride concentration (0-10 ppm), as the ammonium chloride concentration was required for the ammonia concentration calculation.

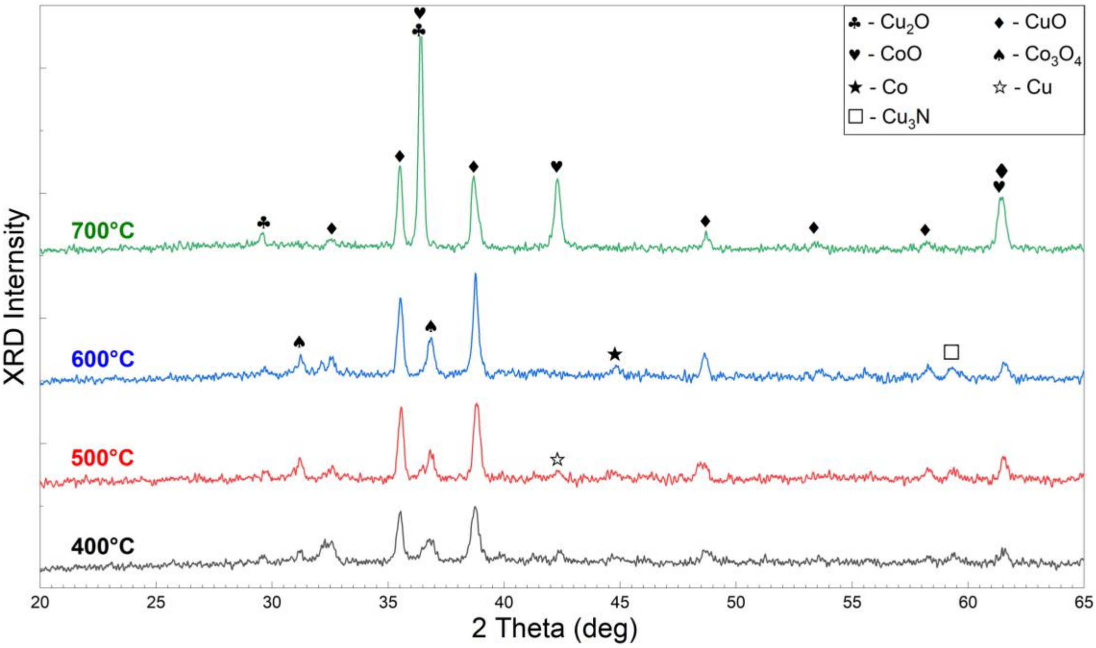

Figure 1 XRD pattern of electrospun fibers calcined at different temperatures.

Results and Discussion

Characterization of fibers

From XRD pattern of the calcined fibers (see **Figure 1**), the major and secondary phases were analyzed as shown in **Table 1**. From **Figure 1**, the XRD patterns of fibers calcined at 400 to 600°C were similar in terms of phases, however, the portions of the phases were different. The primary phase was CuO (COD-7212242 and PDF 04-007-1375) and the secondary phase Co_3O_4. (COD 9005888 and PDF 01-076-1969). The portion of Co_3O_4 increased with the increase of calcination temperature. While Co_3O_4 was not identified for fibers calcined at 700°C, CoO (COD-9008618 and PDF 01-071 1178) was identified instead. This was likely due to the reduction of Co_3O_4 at 700°C. The portion of CoO was higher than CuO, so the CoO become the primary phase for this fiber. In addition, CuO was also reduced to Cu_2O (COD-9007497 and PDF 00-005-0667) at 700°C.

The mixed phases at atmospheric equilibrium are likely Co_3O_4 and (Cu,Co)O, while with a reducing atmosphere, they are likely to be Cu_2O and (Cu,Co)O [10]. At 600°C and below, the heating time was not long enough for N_2 flow to reduce the oxygen content, so similar to calcination in air, the phases in the fibers were oxides. With longer heating and flowing N_2 time, at 700°C, the reduced phases were found.

The specific surface area of calcined fibers was measured and plotted against the calcination temperature (see **Figure 2**). When the temperature increased from 400 to 500°C, the surface area was slightly higher (from 7.24 to 7.61 m^2/g) but when the temperature increased further to 600°C, the surface area decreased (from 7.61 to 4.69 m^2/g). The area decreased more with the temperature of 700°C (from 4.69 to 0.73 m^2/g).

Table 1 Analyzed phases of fibers after calcination at different temperatures.

Calcination Temperature (˚C)	Primary Phase	Secondary Phase
400	CuO	Co_3O_4
500	CuO	Co_3O_4
600	CuO	Co_3O_4
700	CoO	$CuO+Cu_2O$

From SEM image of the calcined fibers (see **Figure 3**), it was seen that the fibers calcined at 400 and 500°C, had nano-scale particle sizes. Short, nano-whiskers, 200 to 250 nm in diameter, were also observed in the fiber microstructure at 600 and 700°C (arrows in **Figure 3** indicate the observed whiskers). These images explain the specific surface area of the calcined fibers. The high surface area of the fibers calcined at 400 and 500°C was likely because of the fine particle size and/or fragmentation of the calcined fiber, while the reduced surface area for fibers calcined at higher temperatures was because of powder densification. For the fiber calcined at 700°C, continued powder densification and whisker growth from 600 to 700°C, led to the lowered surface area.

NtRR catalytic efficiency

From cyclic voltammetry, the potential of -1.3 V was determined to use in the nitrate reduction reaction experiment. The ammonia yield rate of the mixed-oxide fibers was calculated and compared with an electroplated bimetallic catalyst, as shown in **Figure 4**. For the specimen calcined at 400°C, ammonia yield was unable to be measured, for unknown reasons. The yield rate of the fiber calcined at 500°C was comparable to the Cu/Co bimetallic catalyst. The yield rate was much higher for the 600°C calcined fiber, 18 times greater than the electroplated catalyst, however, the rate was lower when temperature was increased to 700°C.

The fiber calcined at 700°C potentially contained a higher amount of CoO and a lower amount of CuO, while the fiber calcined at 600°C contained a higher amount of CuO. This probably indicated that the CuO and Co_3O_4 played a role in NtRR. This higher oxidation state of copper and (Cu^{2+} vs. Cu^{+}) cobalt (Co^{2+} vs. Co^{2+}/Co^{3+}) can perhaps provide more charge transfer for NtRR [4]. As shown in **Figure 4**, the Faradaic efficiency (FE) of the fiber calcined at 600°C was highest and for the fiber calcined at 700°C, was reduced drastically. The resulting yield rate of ammonia in the NtRR was likely a result of the content of suitable oxide catalysts.

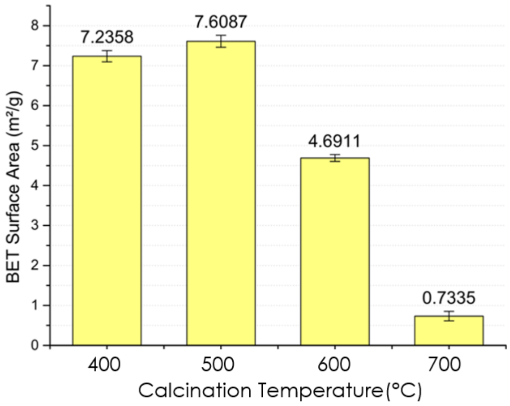

Figure 2 Surface area of fibers calcined at different temperatures.

For CuO, the energy needed to move electrons is more than for Cu_2O. However, the Faradaic efficiency of the fiber calcined at 700°C was smaller when compared to the 600°C calcination temperature. This was likely because the fiber,

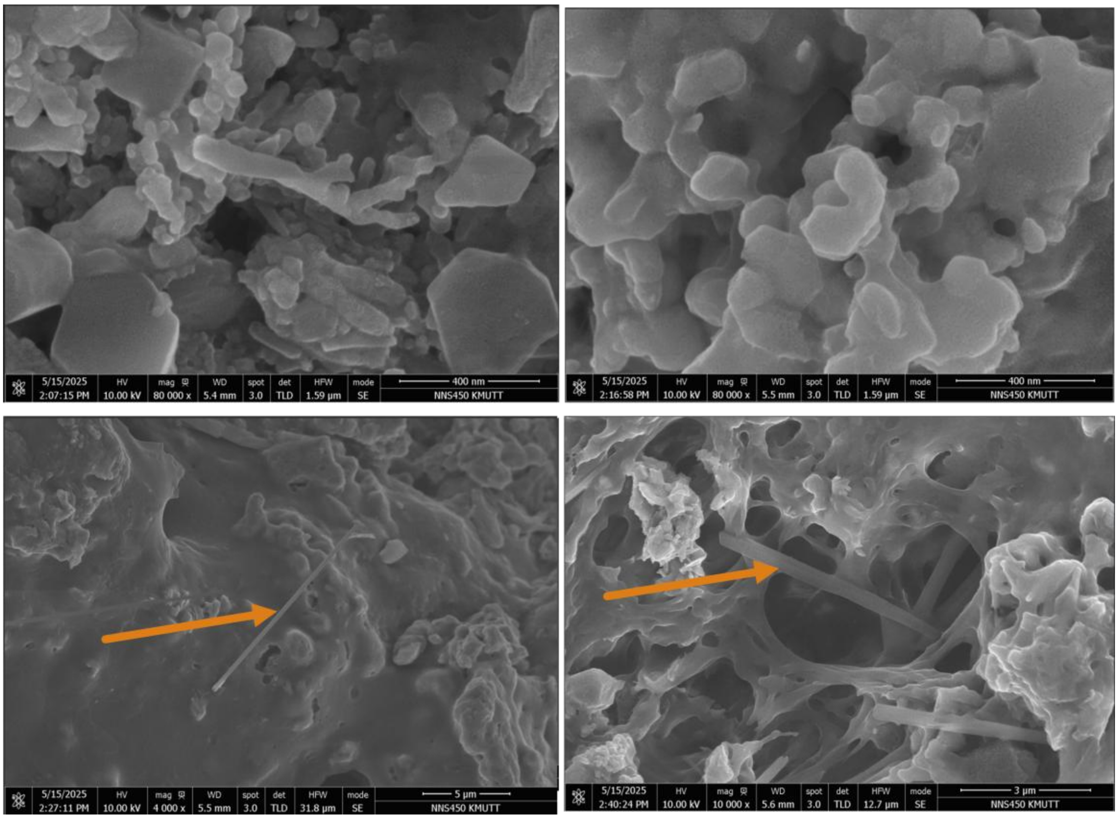

Figure 3 SEM images of electrospun fibers calcined at 400°C (top left), 500°C (top right), 600°C (bottom left), and 700°C (bottom right). Note the different magnifications.

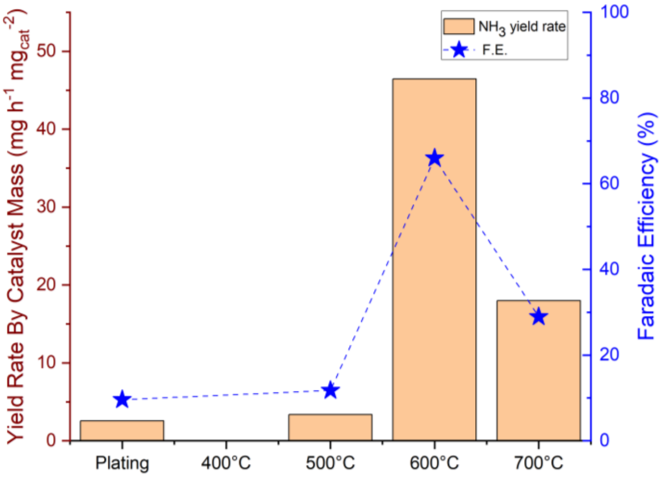

Figure 4 NtRR yield rate and Faradaic efficiency of fibers calcined at different temperatures and an electroplated bimetallic catalyst.

calcined at 600°C, had greater surface area and so the number of active sites was higher and so the Faradaic efficiency was higher.

A Cu_2O film was reported as an efficient electrocatalyst for the nitrate-to-ammonia reduction [11], however, the amount of Cu_2O in fibers calcined at 700°C was not high enough; moreover, the surface area of the fiber was lessened due to densification and whisker growth. Thus, the ammonia yield and the Faradaic efficiency of the fiber calcined at 700°C was lessened. However, the values were still higher than the electroplated Co/Cu catalyst. It yielded ammonia 7 times greater than the electroplated Co/Cu catalyst when compared by catalyst mass.

The copper oxide (CuO) with the cobalt oxide (Co_3O_4) had a synergistic effect, in which the copper oxide had a high catalytic effect and the cobalt oxide absorbed H*, helping the hydrogenation in NtRR [12]. Though, in other research, Co_3O_4 was concluded to be a stable and steady catalyst for both deoxygenation and hydrogenation [13]. The combination of copper oxide and cobalt oxide seems to assist catalytic efficiency through the oxygen vacancies of both. Cobalt (II, III) oxide (Co_3O_4) contains both Co^{2+} and Co^{3+} which can give 2 and 3 e^-, respectively. The possible substitution of Co^{3+} by Cu^{2+} in octahedral sites can create oxygen vacancies in the structure, [14], offering an explanation why the Co_3O_4-containing fiber obtained at 600°C showed the high catalytic effect and high Faradaic efficiency.

Conclusion

In this study, fibers of mixed oxides (copper oxide and cobalt oxide) was fabricated via the calcination of electrospun fibers containing copper and cobalt. The electrospun fibers were calcined at different temperatures to reveal the effect on catalytic efficiency in a nitrate reduction reaction. After calcination at 400 to 600°C, CuO and Co_3O_4 oxides were found in the fibers, while at 700°C, Cu_2O, CuO, and CoO were found. Nano-whiskers were only found when the calcination temperature was at least 600°C or greater. The ammonia yield rate and Faradaic efficiency were the highest for fibers calcined at 600°C, and this was because of the high surface area of the fiber and the synergistic effect of the mixed oxides on hydrogenation and deoxygenation reactions to convert nitrate to ammonia. The fiber calcined at 700°C had reduced surface area, and CoO was found instead of Co_3O_4, so the ammonia yield rate and the Faradaic efficiency were lowered.

From this study, it was concluded that there is the potential to use mixed-oxide fibers as a catalyst in the nitrate reduction reaction (NtRR) to reduce nitrate in polluted water and to produce ammonia at the same time.

Acknowledgements

This study was kindly supported by the Department of Chemical Engineering, Faculty of Engineering, and the Department of Physics, Faculty of Science, at King Mongkut's University of Technology Thonburi (KMUTT).

References

1. A. Wu, *et al.*, Boosting electrocatalytic nitrate-to-ammonia conversion via plasma enhanced CuCo alloy–substrate interaction, *ACS Sustain. Chem. Eng.,* Vol. 10(44), 14539–14548 (2022).
2. M. Figueiredo and I. Katsounaros, Nitrate reduction on noble metal electrodes, In *Encyclopedia of Interfacial Chemistry*, Elsevier, Oxford, 761-768 (2018).
3. G. Quoie, *et al.*, Advancements in catalysts for electrochemical nitrate reduction: A sustainable approach for mitigating nitrate pollution: A review, *Mod. Res. Catal.*, Vol. 13(1) 1-28 (2024).
4. K. Jeon, *et al.*, Recent development of catalysts for the nitrate reduction reaction: Electrochemical solution to produce ammonia, *Top. Catal.*, Vol. 67(19-20), 4-6 (2024).
5. S. Zhang, *et al.*, Fe/Cu diatomic catalysts for electrochemical nitrate reduction to ammonia, *Nat. Commun.*, Vol. 14(1), 3634 (2023).
6. J. Suh, *et al.*, Tandem electroreduction of nitrate to ammonia using a cobalt-copper mixed single-atom/cluster catalyst with synergistic effects, *Adv. Sci*, e2407250 (2024).
7. W. Jung and Y. Hwang, Material strategies in the electrochemical nitrate reduction reaction to ammonia production, *Mater. Chem. Front.*, Vol. 5, 6803-6823 (2021).
8. S. Nui, Recent progress and challenges in structural construction strategy of metal-based catalysts for nitrate electroreduction to ammonia, *J. Ener. Chem.*, Vol. 86, 69-83 (2023).
9. F. Cao, *et al.*, Electrospinning one-dimensional surface-phosphorized CuCo/C nanofibers for enzyme-free glucose sensing, *New J. Chem.*, Vol. 46(24), 11531-11539 (2022).
10. L. Zabdyr and O. Fabrichnaya, Phase equilibria in the cobalt oxide-copper oxide system, *J. Phase Equilib.*, Vol. 23, 149-155 (2002).
11. D. Anastasiadou, *et al.*, Morphology changes of Cu_2O catalysts during nitrate electroreduction to ammonia, *ChemCatChem*, Vol. 15, e202201503 (2023).
12. J. Wei, *et al.*, Copper-based electro-catalytic nitrate reduction to ammonia from water: Mechanism, preparation, and research directions, *Environ. Sci. & Ecotec.*, Vol. 20, 100383 (2024).
13. K. Yang, *et al.*, Unveiling the reaction mechanism of nitrate reduction to ammonia over cobalt-based electrocatalysts, *J. Am. Chem. Soc.,* Vol. 146(19), 12976-12983 (2024).
14. M. Ahmed, *et al.*, Tailoring surface electronic structure of spinel Co_3O_4 oxide via Fe and Cu substitution for enhanced oxygen evolution reaction, *ACS Mater. Lett.*, Vol. 6(10), 4756-4764 (2024).

Influence of Synthesis Method on the Structural and Visible-Light Photocatalytic Activity of $BiVO_4$

P. Lainok[1], W. Reainthippayasakul[1,2], N. Jiraborvornpongsa[2,3], P. Sujaridworakun[1,2,4,*]
[1] Department of Materials Science, Faculty of Science, Chulalongkorn University, Bangkok, 10330, Thailand
[2] Photocatalysts for Clean Environment and Energy Research Unit, Faculty of Science, Chulalongkorn University, Bangkok, 10330, Thailand
[3] Metallurgy and Materials Science Research Institute, Chulalongkorn University, Bangkok, 10330, Thailand
[4] Center of Excellence on Petrochemical and Materials Technology, Chulalongkorn University, Bangkok, 10330, Thailand
* pornapa.s@chula.ac.th

Abstract

Bismuth vanadate ($BiVO_4$) has emerged as a promising visible-light photocatalyst owing to its narrow band gap (2.4 eV), excellent chemical stability, and earth-abundant elemental composition. However, the photocatalytic efficiency of $BiVO_4$ is strongly dependent on its structural and morphological characteristics, which are significantly influenced by synthesis methodology. This study presents a systematic investigation of $BiVO_4$ photocatalysts prepared via three distinct synthesis routes: hydrothermal, solvothermal, and liquid-solid reaction synthesis. The objective was to elucidate structure-activity relationships and identify the optimal synthesis approach for enhanced visible-light photocatalytic performance. Comprehensive characterization was performed using X-ray diffraction (XRD) for crystalline phase identification and structural analysis, scanning electron microscopy (SEM) for morphological evaluation, and Brunauer-Emmett-Teller (BET) surface area analysis for determining specific surface area. Photocatalytic activity was evaluated through Rhodamine B (RhB) degradation under simulated visible light irradiation ($\lambda > 420$ nm) as a model pollutant system. The results demonstrated that the synthetic method significantly affects the photocatalytic efficiency of $BiVO_4$, primarily through variations in surface area, particle dispersion, and light absorption properties. These findings provide crucial insights into the synthesis-structure-performance relationships in $BiVO_4$ photocatalysts and establish a foundation for rational design of efficient visible-light-driven photocatalytic systems for environmental remediation and solar fuel production applications. Future work will focus on improving charge separation efficiency and long-term operational stability under visible-light exposure.

Keywords: Bismuth Vanadate; Hydrothermal; Solvothermal; Liquid-Solid Reaction; Dye Degradation

---

Introduction

In the present scenario, the conventional energy sources such as coal and petroleum products are nearly depleted due to massive utilization, expanding industrialization, and rapid population growth. Consequently, the demand for clean and sustainable energy production and environmental conservation technology is increasing drastically. According to reports, air pollution ranks fourth on the global risk factors, contributing to almost five million deaths worldwide each year. Additionally, the massive discharge of toxic and carcinogenic industrial wastes such as synthetic dyes, antibiotics, pesticides and heavy metals/fluorides into water reservoirs poses a serious threat to both aquatic and human life [1]. The energy needs of society required to maintain and expand the living standards and well-being of a growing human population represent a major, urgent and global challenge facing mankind in the 21st century. Moreover, this challenge must be met without excessive use of fossil fuels, as carbon emissions are believed to be the main driver of deleterious climate change [2]. As both global energy consumption and concerns over environmental contamination continue to increase, it is imperative to develop renewable energy resources that neither rely on fossil fuels nor emit carbon dioxide. Solar energy has attracted much interest as one such sustainable, clean energy source [3], being recognized as a primary renewable energy source that can be employed for producing clean and sustainable hydrogen with the potential to play a vital role in the transition from conventional to renewable energy sources [4].

The growing demand for sustainable and energy-efficient environmental remediation technologies has driven research toward clean energy-driven processes. Heterogeneous photocatalytic degradation has emerged as a promising advanced oxidation process that harnesses light energy to activate semiconductor materials, generating highly reactive oxygen species capable of completely mineralizing organic contaminants into harmless products such as CO_2 and H_2O without secondary pollution [5]. Photocatalysis offers significant advantages including ambient temperature and pressure operation, potential utilization of abundant solar energy, and elimination of chemical additives, making it an environmentally benign and sustainable technology [6]. The development of visible-light-responsive photocatalysts is particularly crucial as visible light constitutes approximately 43% of the solar spectrum, offering tremendous potential for solar-driven photocatalytic applications that can operate without external energy input [7, 8].

Bismuth vanadate ($BiVO_4$) has attracted considerable attention as a promising visible-light-responsive photocatalyst owing to its optimal band gap energy of approximately 2.4 eV, excellent photochemical stability, non-toxic nature, and earth-abundant constituent elements [9]. $BiVO_4$ exists in three main crystalline polymorphs, among which the monoclinic scheelite structure exhibits superior photocatalytic activity due to enhanced charge carrier mobility and prolonged electron-hole separation [10]. However, the photocatalytic performance of $BiVO_4$ is critically dependent on its physicochemical properties, including crystallinity, morphology, particle size, and specific surface area, all of which are strongly influenced by the synthesis methodology employed [11].

Various synthesis routes have been developed for $BiVO_4$ preparation, including hydrothermal, solvothermal, solid-state, and liquid-solid reaction methods. Each technique operates under different reaction conditions and offers distinct advantages in controlling particle characteristics, thereby influencing photocatalytic efficiency [12]. The hydrothermal method, conducted in aqueous media under elevated temperature and pressure, typically produces well-crystallized particles with good dispersibility. The solvothermal method, utilizing organic solvents, offers advantages in controlling particle morphology through solvent effects. The liquid-solid reaction method provides a simple approach but often results in larger particle sizes due to limited mass transport compared to solution-based methods [13, 14].

This study systematically investigated the influence of three different synthesis methods hydrothermal, solvothermal, and liquid-solid reaction on the structural properties and visible-light photocatalytic activity of $BiVO_4$ for Rhodamine B degradation as a model pollutant. The findings provide valuable insights into synthesis-structure-performance relationships and establish guidelines for optimizing $BiVO_4$ photocatalyst design for sustainable environmental remediation using clean solar energy.

Materials and Methods

Materials

In the synthesis of $BiVO_4$ via the hydrothermal methods, bismuth nitrate pentahydrate ($Bi(NO_3)_3\cdot 5H_2O$, Sigma-Aldrich, ≥98%), ammonium metavanadate (NH_4VO_3, Ajax Finechem, 99%), nitric acid (HNO_3, Merck, 65%), and ammonia solution (NH_3(aq.), Qrëc, 25% AR Grade) were used. The solvothermal method employed the same bismuth and vanadium precursors along with additional reagents including sodium hydroxide (NaOH, Qrëc, 99% AR Grade) and ethanol (C_2H_5OH, Merck, ≥99.9%). For the liquid-solid reaction synthesis, bismuth oxide (Bi_2O_3, Qrëc, 99.5% AR Grade) and vanadium pentoxide (V_2O_5, Kanto Chemical, 99%) were utilized as precursors. In the assessment of Photocatalytic efficiency for dye degradation, Rhodamine B (RhB, Loba Chemie) was employed as the chosen dye. Deionized water was used throughout all experiments. All chemicals were of analytical grade and used without further purification.

Sample preparation

Hydrothermal method (HT): 1.4552 g of bismuth nitrate pentahydrate ($Bi(NO_3)_3\cdot 5H_2O$) was dissolved in 30 ml of 2 M nitric acid (HNO_3), while 0.3549 g of ammonium metavanadate (NH_4VO_3) was separately dissolved in 30 ml of deionized water, maintaining a bismuth to vanadium mole ratio of 1:1. The two solutions were mixed and stirred for 60 minutes to form a homogeneous yellow suspension. Ammonia solution (NH_3(aq.)) was added dropwise to adjust the pH to 7, followed by additional stirring for 30 minutes. The mixture was transferred to a 100 ml Teflon-lined autoclave and heated at 200°C for 6 hours. After cooling to room temperature, the resulting precipitate was filtered, washed with deionized water and ethanol, and dried at 80°C for 24 hours.

Solvothermal method (ST): 1.4552 g of $Bi(NO_3)_3\cdot 5H_2O$ was dissolved in a mixture of 23 ml ethanol and 7 ml of 2 M HNO_3, while 0.3549 g of NH_4VO_3 was dissolved in 30 ml of 3 M sodium hydroxide (NaOH) solution, maintaining a bismuth to vanadium mole ratio of 1:1. After mixing the two solutions, the mixture was stirred for 60 minutes. Then, 2 M HNO_3 was added dropwise to adjust the pH to 1, followed by stirring for 30 minutes. The solution was transferred to a 100 ml Teflon-lined autoclave and heated at 130°C for 4 hours. After cooling to room temperature, the resulting product was filtered, washed thoroughly with deionized water and ethanol, and dried at 80°C for 24 hours.

Liquid-solid reaction method (LSR): 13.979 g of bismuth oxide (Bi_2O_3) and 5.456 g of vanadium pentoxide (V_2O_5) powders were used as precursors, maintaining a bismuth to vanadium mole ratio of 1:1. The mixed powders were dissolved in 300 ml of 0.8 M HNO_3 and stirred for 15 minutes, then heated in oil bath at 80°C for 48 hours. After cooling to room temperature, the resulting $BiVO_4$ powder was filtered, washed thoroughly with deionized water and ethanol, and dried at 80°C for 24 hours.

Characterization

The crystal structures of the products were characterized using X-ray diffractometer (XRD; Bruker AXS Model D8 Discover, Germany) with Cu Kα radiation at 40 kV and 40 mA (λ =1.5406 Å). The crystallite size was determined employing the Scherrer equation in Equation (1):

$$D = \frac{k\lambda}{\beta cos\theta} \quad (1)$$

Here, D denotes the average crystallite size (nm), k is the shape factor (k = 0.90 used for spherical crystallites), λ is the X-ray wavelength (λ = 0.15406 nm), β is the full width at half maximum (FWHM) of the peak (radians), and θ is the Bragg-diffraction angle (radians).

The morphology of the powder was observed by a Scanning Electron Microscope (JEOL JSM-6480LV) at an acceleration voltage of 15.0 kV.

The specific surface area of the samples was analyzed using a surface area analyzer (Micromeritics 3Flex 3500) measured by N_2 adsorption at 77 K. Before analysis, sample preparation involved degassing at 100°C for 5 hours through heating and evacuation. The specific surface area was determined using the Brunauer-Emmett-Teller (BET) method.

Photocatalytic efficiency evaluation

Photocatalytic dye degradation efficiency was assessed through rhodamine B degradation under a visible light source (500 W Xe lamp equipped with UV cut-off filter) positioned 10 cm away. A 0.05 g photocatalyst was ultrasonicated in 10 ppm rhodamine B solution (120 ml) for 5 minutes. Preceding light irradiation, the suspension was stirred with a magnetic stirrer in the dark for 30 minutes to attain adsorption-desorption equilibrium. Visible light exposure followed for 2 hours, with 5 ml solution samples collected every 15 minutes during both dark and light conditions. After centrifugation to remove the catalyst, concentration analysis was conducted using a UV–Vis–NIR spectrophotometer (Agilent Cary 7000 UMS) at the maximum absorbance wavelength of 554 nm. The dye degradation efficiency of the samples was determined using Equation (2):

$$Dye\ degradation\ efficiency(\%) = \frac{C_D - C}{C_D} \times 100 \quad (2)$$

where C_D is the dye concentration after being kept in the dark (mg·L^{-1}), and C is the dye concentration at each irradiated time (mg·L^{-1}).

Results and Discussion

Structural characterization

XRD analysis revealed that the synthesis method significantly influences the crystal phase composition of $BiVO_4$ (Figure 1). Both hydrothermal (HT) and liquid-solid reaction (LSR) methods successfully produced pure monoclinic scheelite $BiVO_4$ (JCPDS No. 00-044-0081), as evidenced by characteristic diffraction peaks at 2θ values of approximately 18.7°,19.0°, 29.0°, 30.5°, 34.5°, 35.2°, 39.8°, 46.7°, and 47.3° corresponding to the (110), (011), (121), (040), (200), (002), (211), (240), and (042) crystal planes, respectively. In contrast, the solvothermal (ST) sample exhibited a mixture of monoclinic and tetragonal phases. The presence of tetragonal dreyerite $BiVO_4$ (JCPDS No. 00-014-0133) was identified by the characteristic peaks at 2θ ≈ 24.4°, 32.7° and 48.4° which corresponds to the (200), (112) and (312) planes of the tetragonal structure, respectively. This mixed-phase formation can be attributed to the use of ethanol as solvent and the lower synthesis temperature (130°C) compared to the hydrothermal method (200°C), which may not provide sufficient energy for complete transformation to the thermodynamically more stable monoclinic phase.

The pH conditions during synthesis critically influenced phase composition. The neutral pH (pH 7) in the hydrothermal method promoted simultaneous precipitation and thermodynamically controlled formation of pure monoclinic $BiVO_4$ at 200°C. In contrast, the solvothermal method was designed to operate at pH 1 for precursor dissolution. At strongly acidic condition, kinetically controlled nucleation dominated, promoting the formation of metastable tetragonal dreyerite phase. During subsequent solvothermal heating, partial structural rearrangement toward the thermodynamically stable monoclinic scheelite phase could occur. Thus, the coexistence of monoclinic and tetragonal phases occurred from the competition between rapid precipitation of tetragonal phase at very low pH and slower thermodynamic transformation of monoclinic phase.

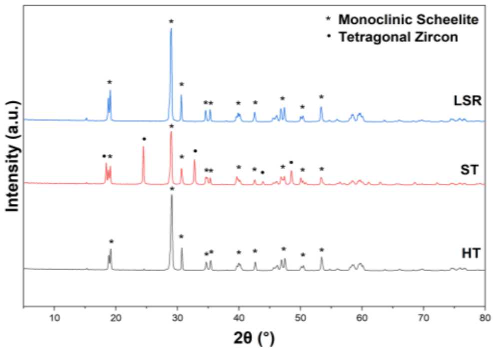

Figure 1 XRD patterns of $BiVO_4$ with different synthesis methods.

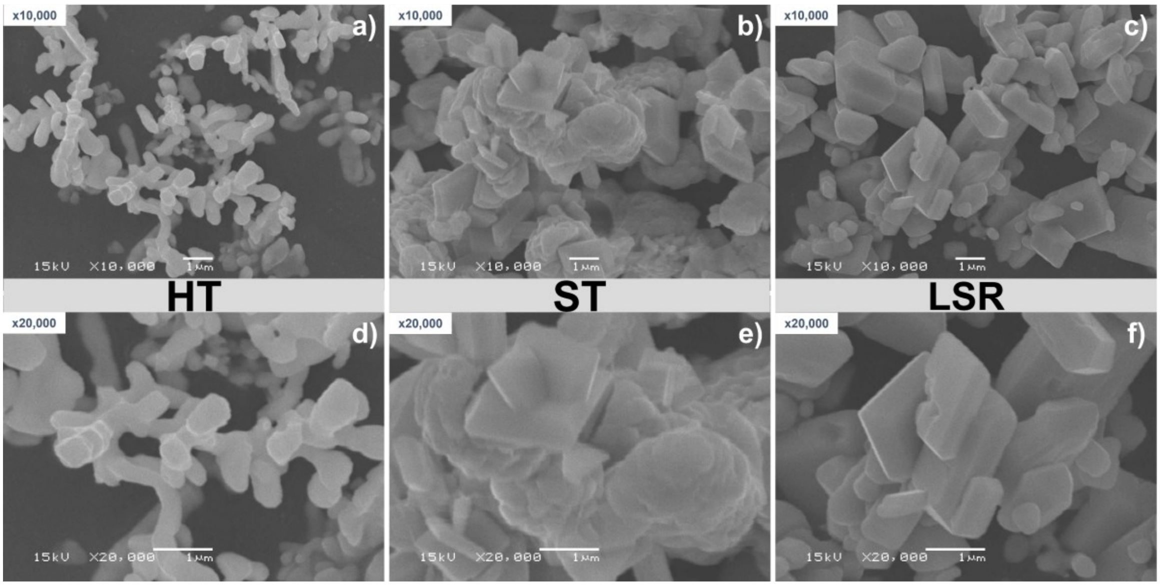

Figure 2 SEM images of $BiVO_4$ particles: a) HT, b) ST, and c) LSR at 10,000x magnification, and d) HT, e) ST, and f) LSR at 20,000x magnification.

The sharp and well-defined peaks in all samples indicate high crystallinity of the synthesized $BiVO_4$ samples.

Crystallite sizes calculated from the Scherrer equation using the (121) peak at $2\theta \approx 29.0°$ (Table 1) revealed subtle differences among the methods: HT (2.812 nm), ST (3.060 nm), and LSR (3.008 nm). The result showed that the hydrothermal method produced the smallest crystallite size, which can be attributed to the higher synthesis temperature (200°C) promoting better crystallization dynamics and uniform nucleation.

Table 1 Calculated crystallite size of the $BiVO_4$

Sample	Crystallite size (nm)
HT	2.812
ST	3.060
LSR	3.008

Morphological analysis

SEM images (Figure 2) revealed distinct morphological differences among the three synthesis methods. The hydrothermal sample exhibited relatively uniform, well-dispersed particles with irregular polyhedral shapes. The solvothermal sample showed agglomerated particles with less defined boundaries, potentially due to the use of organic solvent affecting particle growth kinetics. The liquid-solid reaction sample displayed larger, more aggregated particles with heterogeneous size distribution, consistent with solid-phase reaction mechanisms that typically produce fewer uniform morphologies.

BET surface area analysis

BET surface area measurements (Table 2) showed significant variation depending on synthesis method: HT (1.9727 m^2/g), ST (1.6050 m^2/g), and LSR (0.7938 m^2/g). The hydrothermal method yielded the highest specific surface area, approximately 2.5 times greater than the liquid-solid reaction method. Higher surface area provides more active sites for photocatalytic reactions and facilitates better contact between the catalyst and target pollutants.

The superior surface area of the hydrothermal sample can be attributed to the aqueous medium and controlled temperature-pressure conditions in the autoclave, which promote formation of smaller, less agglomerated particles. The significantly lower surface area of the liquid-solid reaction sample reflects the limited mass transport and higher particle sintering tendency results in larger crystallites.

Table 2 BET surface area of the $BiVO_4$

Sample	Surface Area (m^2/g)
HT	1.9727
ST	1.6050
LSR	0.7938

Photocatalytic activity

Photocatalytic degradation experiments (Figure 3) demonstrated that the HT sample exhibited the highest Rhodamine B degradation efficiency (17.27%) under visible light irradiation for 2 h, followed by the LSR (9.91%) and the ST (8.31%) samples. This trend correlates well with the BET surface area results, confirming that a higher surface area enhances photocatalytic activity by providing more active sites and improving light utilization.

The superior performance of the HT sample can be attributed to its highest specific surface area, better particle dispersion, and favorable crystallite size, which collectively promote efficient charge separation and suppress electron-hole recombination. In contrast, the lower photocatalytic activity of the ST sample is mainly associated with its mixed monoclinic-tetragonal phase composition and reduced surface area. The presence of mixed phases may introduce phase boundaries that act as recombination centers, while the lower surface area (1.6050 m²/g compared to 1.9727 m²/g for HT) limits the number of available active sites. The combined effect of these factors results in inferior photocatalytic degradation efficiency for the ST sample (8.31% compared to 17.27% for HT).

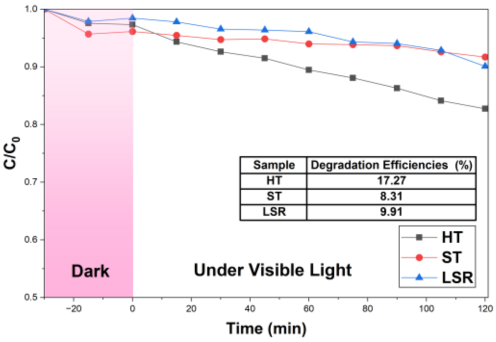

Figure 3 Photocatalytic degradation of Rhodamine B in the presence of $BiVO_4$ samples

Conclusion

This study systematically investigated the influence of three synthesis methods on the structural properties and photocatalytic activity of $BiVO_4$. All synthesis methods produced crystalline $BiVO_4$, although with different phase compositions: the hydrothermal and liquid-solid reaction methods yielded pure monoclinic phase, while the solvothermal method resulted in a mixture of monoclinic and tetragonal phases. The hydrothermal method demonstrated superior performance, yielding the highest BET surface area (1.9727 m²/g) and consequently the best photocatalytic degradation efficiency for Rhodamine B (17.27%) under visible light irradiation for 2 h. The results establish a clear structure-activity relationship, demonstrating that synthesis methodology is a critical parameter for optimizing $BiVO_4$ photocatalyst performance. These findings provide valuable insights for the rational design of efficient $BiVO_4$-based photocatalytic systems for environmental remediation applications.

Acknowledgements

The authors gratefully acknowledge the Department of Materials Science, Faculty of Science, Chulalongkorn University for providing research facilities and support.

References

1. S. Das, et al., A critical review on prospects and challenges of metal-oxide embedded g-C3N4-based direct Z-scheme photocatalysts for water splitting and environmental remediation. *Applied Surface Science Advances*, Vol. 11, 100273 (2022).
2. W. Zhao, et al., Photocatalytic overall water splitting endowed by modulation of internal and external energy fields. *Chemical Science*, Vol. 15(42), 17292-17327 (2024).
3. Q. Wang, K. Domen, Particulate Photocatalysts for Light-Driven Water Splitting: Mechanisms, Challenges, and Design Strategies. *Chem Rev*, Vol. 120(2), 919-985 (2020).
4. I. Dincer, H. Ishaq, Solar Energy-Based Hydrogen Production. *Renewable Hydrogen Production*, 91-122 (2022).
5. A. Fujishima, X. Zhang, D. A. Tryk, TiO_2 photocatalysis and related surface phenomena. *Surface Science Reports*, Vol, 63(12), 515-582 (2008).
6. S. Ahmed, et al., Heterogeneous Photocatalytic Degradation of Phenols in Wastewater: A Review on Current Status and Developments. *Desalination*, Vol. 261, 3-18 (2010).
7. X. Wang, et al., Full-Spectrum Solar-Light-Activated Photocatalysts for Light-Chemical Energy Conversion. *Advanced Energy Materials*, Vol. 7, 1700473 (2017).
8. L. V. Samarasinghe, S. Muthukumaran, K. Baskaran, Recent advances in visible light-activated photocatalysts for degradation of dyes: A comprehensive review. *Chemosphere*, Vol. 349, 140818 (2023).
9. A. Kudo, K. Omori, H. Kato, A Novel Aqueous Process for Preparation of Crystal Form-Controlled and Highly Crystalline $BiVO_4$ Powder from Layered Vanadates at Room Temperature and Its Photocatalytic and Photophysical Properties. *Journal of the American Chemical Society*, Vol. 121(49), 11459-11467 (1999).
10. S. Tokunaga, H. Kato, and A. Kudo, Selective Preparation of Monoclinic and Tetragonal $BiVO_4$ with Scheelite Structure and Their Photocatalytic Properties. *Chemistry of Materials*, Vol. 13(12), 4624-4628 (2001)..
11. D. Wang, et al., Crystal Facet Dependence of Water Oxidation on $BiVO_4$ Sheets under Visible Light Irradiation. *Chemistry (Weinheim an der Bergstrasse, Germany)*, Vol. 17, 1275-1282 (2001).
12. L. Zhang, D. Chen, X. Jiao, Monoclinic Structured $BiVO_4$ Nanosheets: Hydrothermal Preparation, Formation Mechanism, and Coloristic and Photocatalytic Properties. *The*

Journal of Physical Chemistry B, Vol. 110(6), 2668-2673 (2006).

13. G. S. Kamble, Y. Ling, Solvothermal synthesis of facet-dependent $BiVO_4$ photocatalyst with enhanced visible-light-driven photocatalytic degradation of organic pollutant: assessment of toxicity by zebrafish embryo. *Scientific Reports*, Vol. 10 (2020).
14. A. Iwase, H. Kato, A. Kudo, A Simple Preparation Method of Visible-Light-Driven $BiVO_4$ Photocatalysts From Oxide Starting Materials (Bi_2O_3 and V_2O_5) and Their Photocatalytic Activities. *Journal of Solar Energy Engineering*, Vol. 132(2) (2010).

Preparation of Zeolite 13X from Ceramic Wastes for Carbon Dioxide Capture

Kittiphum Wong [1,*], Nathakon Nakpao [1], and Thanakorn Wasanapiarnpong[1,2]
[1] Department of Materials Science, Faculty of Science, Chulalongkorn University, Phayathai Road, Pathumwan, Bangkok 10330, Thailand
[2] Upcycled Materials from Industrial and Agricultural Wastes Research Unit, Department of Materials Science, Faculty of Science, Chulalongkorn University, Phayathai Road, Bangkok, 10330, Thailand
*Corresponding author e-mail address: w.kittiphum9@gmail.com

Abstract

This research aims to study the synthesis of 13X zeolite from ceramic pitcher waste materials, including pitcher porcelain sanitaryware, porcelain insulators, pitcher porcelain tableware, and pottery stone. The main objective was to reuse these waste materials as carbon dioxide (CO_2) absorbents, a major greenhouse gas contributing to global warming. The zeolite was synthesized via a hydrothermal method in which 100 g of finely ground ceramic pitchers and pottery stone were mixed with 120 g of sodium hydroxide (NaOH) powder and calcined at 800 °C at a heating rate of 5 °C/min for 2 hours. The calcined product was then mixed with purified water (RO) at a ratio of 1:4 by weight and incubated at 90 °C for 24 hours to induce zeolite crystallization. The synthesized products were characterized using X-ray diffraction (XRD), scanning electron microscopy (SEM), and Brunauer Emmett Teller (BET) specific surface area analysis. The sanitaryware-based zeolite exhibited the highest specific surface area of 521.03 m^2/g, with diffraction patterns confirming the formation of Zeolite 13X with good crystallinity and suitable for CO_2 adsorption. The obtained zeolite powders were then formed into 10 mm diameter spherical pellets using a meta-kaolin based geopolymer binder. A zeolite to geopolymer ratio of 50:50 by weight gave the optimum results, with a maximum strength of 10.19 N after forming. the zeolite pellets retain a specific surface area of 398.64 m^2/g and can adsorb 2.37 mmol/g of CO_2, equivalent to 10.43 wt%. First comparative ranking of 4 ceramic wastes and novel geopolymer pellets enable industrial CO_2 capture from landfill waste. This research indicates the potential for converting ceramic waste into Zeolite 13X, which has efficient CO_2 adsorption properties. The proposed process is not only a low-cost and industrially scalable synthesis method but also supports the circular economy concept by converting non-biodegradable waste into value-added materials.

Keywords: Zeolite 13X; Ceramic pitcher waste; Carbon dioxide capture; Geopolymer

---

ccc

As climate change intensifies due to the accumulation of greenhouse gases, particularly carbon dioxide (CO_2), the development of carbon capture and storage technologies has become increasingly urgent. Cost-effective yet efficient adsorbent materials are critical to such systems. Zeolite 13X, which possesses a FAU-type porous structure with pore sizes of approximately 10 Å, represents an outstanding material for CO_2 adsorption [3][7]. However, conventional synthesis routes using pure precursors remain relatively expensive [7]. This research proposes upcycling "ceramic waste" into resources for producing zeolite 13X. Four types of raw materials including ceramic waste were selected: pottery stone, porcelain insulators pitcher, porcelain tableware pitcher, and vitreous china sanitaryware pitcher. All non-biodegradable wastes whose quantities are increasing and typically end up in landfills, despite their composition being rich in SiO_2 and Al_2O_3, making them highly suitable for constructing aluminosilicate zeolite frameworks [1,5]. The research approach focuses on developing optimal hydrothermal conditions (liquid-to-solid ratio, temperature, time, and alkalinity) to transform waste materials into the 13X phase, followed by forming geopolymer binders to enhance mechanical strength and practical usability. Properties were evaluated using XRD, SEM, and BET analyses, coupled with CO_2 adsorption-desorption performance testing of both powder and formed pellets, including assessment of recyclability. The expected outcomes include reducing landfill burdens and supporting CO_2 emission reduction in practical applications, obtaining cost-effective adsorbent materials from waste, while establishing a scalable circular economy model applicable at both community and industrial levels.

Materials and Methods

The synthesis procedure consisted of four main stages: alkaline fusion, hydrothermal crystallization, washing and purification, and drying

Material Preparation and Alkaline Fusion

Each ceramic raw material was ground using a vibratory disc mill for 2 minutes to obtain fine powder passing through a 100-mesh sieve. Subsequently, 100 g of ceramic powder was mixed with 120 g of NaOH flakes and milled for an additional 1 minute to ensure homogeneous distribution. The mixture was then transferred to high-alumina ceramic crucibles and subjected to calcination in a muffle furnace at 800 °C with a heating rate of 5 °C/min, maintaining the peak temperature for 2 hours. After calcination, the fused product was ground again for 1 minute to break up agglomerates and enhance reactivity for the subsequent hydrothermal step.

Hydrothermal Crystallization

100 g of alkali-fused powder was mixed with 400 g of reverse osmosis (RO) water in a beaker and stirred using a magnetic stirrer for 30 minutes to achieve complete dispersion. The beaker was then sealed and placed in an oven at 90°C for 24 hours to promote zeolite crystallization.

Washing and Purification

After the hydrothermal treatment, the solution was allowed to settle, and the clear supernatant was carefully decanted. 500 g of distilled water was added to the precipitate, stirred for 5 minutes, and left to settle for 30 minutes; this washing procedure was repeated five times. The precipitate was then filtered using filter paper and washed with distilled water two additional times until the washing reached neutral pH.

Washing to neutral pH removes excess NaOH and soluble silicates that block micropores (~10 Å), preserving BET surface area and CO_2 adsorption capacity Residual alkali (pH >11) reduces pore accessibility and pellet strength [3][5]**.**

Drying

The purified zeolite precipitate was dried in an oven at 110 °C for 24 hours to completely remove residual moisture.

Pelletization Using Geopolymer Binder

Metakaolin powder was mixed with sodium silicate solution at various ratios, with the 50:50 weight ratio identified as optimal. The synthesized Zeolite 13X powder was then mixed with the geopolymer binder at a 50:50 weight ratio. The mixture was manually formed into spherical pellets approximately 10 mm in diameter. The formed pellets were cured at room temperature for 24 hours to allow complete geopolymerization, followed by drying at 110°C for 24 hours.

Characterization Methods

Results an X-ray diffraction was used to identify crystalline phases and confirm FAU-type zeolite formation. Scanning electron microscopy observations were performed to examine particle morphology and crystal distribution. Brunauer Emmett Teller surface area measurements using nitrogen adsorption desorption were used to assess textural properties. Compressive strength tests were conducted on individual pellets to evaluate mechanical integrity. Carbon dioxide adsorption capacity was determined from equilibrium carbon dioxide uptake of powders and pellets, reported in millimole per gram and weight percent.

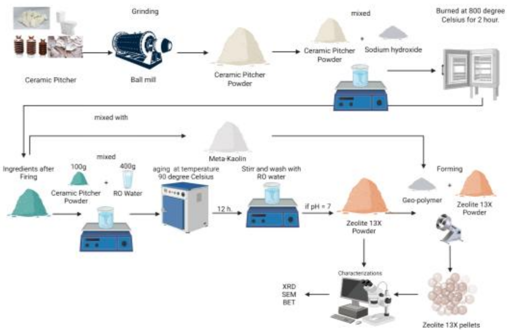

Figure 1 Schematic representation of the Zeolite 13X synthesis process and subsequent palletization using geopolymer binder

Figure 1 illustrates the complete synthesis route from waste grinding to final pellet production, highlighting key process parameters optimized for industrial scalability

Results and Discussion

Crystal Structure Analysis

X-ray diffraction analysis was employed to monitor phase transformation throughout the synthesis process from raw materials to the final product

Raw Material Composition: XRD analysis of the starting materials revealed distinct mineralogical compositions. Pottery stone contained quartz, feldspar, kaolinite, and muscovite, whereas porcelain electrical insulators and sanitaryware exhibited quartz and mullite as the primary phases, the latter formed through high-temperature firing during manufacturing (**Figure 2).**

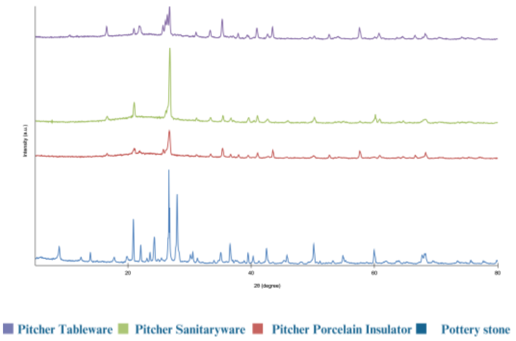

Figure 2 XRD patterns of four types of ceramic waste raw materials.

Post-Fusion Phase After hydrothermal treatment, XRD patterns confirmed the successful formation of Zeolite 13X in all samples. Characteristic peaks appeared at $2\theta \approx 6.2°$, which is diagnostic of the FAU-type framework structure.

Additionally, Zeolite P was detected as a minor secondary phase in small quantities. Upon replicate experiments, the sanitaryware-derived sample displayed the highest peak intensity and sharpness, indicating superior crystallinity and the highest content of Zeolite 13X phase (**Figure 3**).

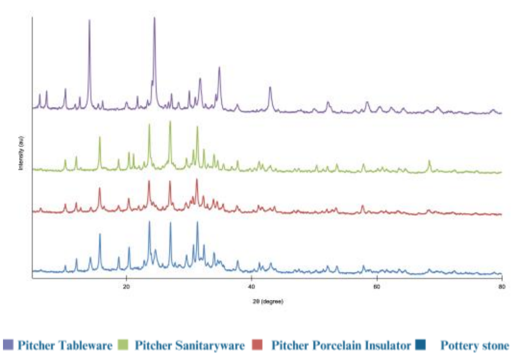

Figure 3 XRD patterns showing the crystalline phases of ceramic waste materials after alkali fusion

Zeolite 13X Crystallization After hydrothermal treatment, XRD patterns confirmed the successful formation of Zeolite 13X in all samples. Characteristic peaks appeared at 2θ ≈ 6.2°, which is diagnostic of the FAU-type framework structure. Additionally, Zeolite P was detected as a minor secondary phase in small quantities. Upon replicate experiments, the sanitaryware-derived sample displayed the highest peak intensity and sharpness, indicating superior crystallinity and the highest content of Zeolite 13X phase (**Figure 4**).

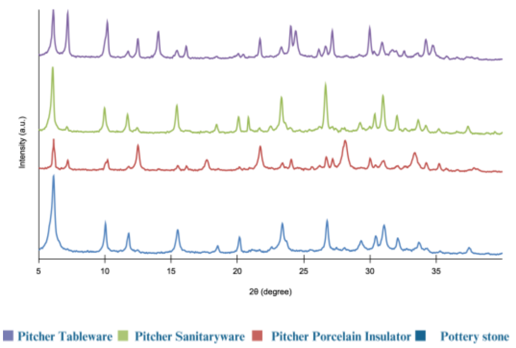

Figure 4 XRD patterns of Zeolite 13X synthesized from four types of ceramic waste materials.

Morphological Analysis

Scanning electron microscopy observations at 20,000X magnification revealed that particles synthesized from all raw materials exhibited densely packed, well-ordered hexagonal to octahedral crystals characteristic of Zeolite 13X morphology (**Figure 5**). The crystal size ranged from approximately 2 to 5 μm with uniform distribution across all samples. The absence of amorphous phases confirms the effectiveness of the synthesis process in completely converting ceramic waste materials into crystalline zeolite, consistent with X-ray diffraction findings. The sanitaryware-derived zeolite exhibited the most regular crystal habits with sharp edges and well-defined facets, indicating optimal crystallization conditions.

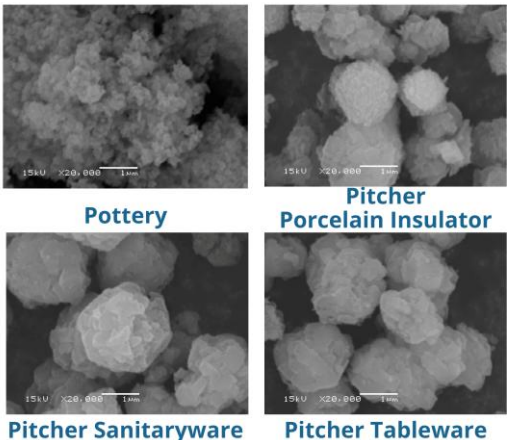

Figure 5 SEM images of Zeolite 13X synthesized from four types of ceramic waste materials at 20,000× magnification.

Specific Surface Area Analysis

Specific surface area, a critical indicator of gas adsorption capacity, varied significantly by precursor. Among triplicate experiments, pottery stone** achieved the highest BET surface area (681.27 m²/g, **Table 1**) due to its kaolinite-rich composition (Si/Al ≈ 2.2) enabling complete alkali fusion, while porcelain sanitaryware reached 521.03 m²/g. both comparable to commercial Zeolite 13X (500-700 m²/g) [4][6] Conversely, porcelain insulators (434 m²/g avg.) and tableware (371 m²/g avg.) showed inferior performance with declining trends, the latter's 347.25 m²/g minimum indicating mullite impurities and suboptimal Si/Al hindering FAU framework formation

Table 1 Surface area of Zeolite 13X synthesized from different ceramic waste materials.

Sample	BET Surface area (m²/g)			
	Trial 1	Trial 2	Trial 3	Average
Pottery Stone	574.43	572.92	681.27	609.54
Pitcher Porcelain Insulator	437.35	431.43	433.82	434.20
Pitcher Porcelain Sanitaryware	405.87	463.45	521.03	463.45
Pitcher Porcelain Tableware	376.20	390.20	347.25	371.22

Geopolymer Binder Optimization

Preliminary screening experiments evaluated various metakaolin to sodium silicate mass ratios for geopolymer binder preparation. A 50:50 weight ratio was identified as optimal, providing balanced rheological properties conducive to pellet formation while ensuring adequate mechanical integrity post-curing. Ratios deviating from this optimum exhibited processing challenges. Formulations with 30:70 metakaolin to sodium silicate demonstrated excessive fluidity with incomplete mixing and inadequate green strength, while 40:60 compositions yielded inhomogeneous textures and poor workability. The selected 50:50 formulation exhibited appropriate viscosity for manual forming operations and developed sufficient cohesive strength during the initial curing period.

Mechanical Strength of Zeolite Pellets

Compressive strength testing revealed an inverse relationship between zeolite content and mechanical performance (**Figure 5**). Pellets containing 20 to 30 wt% zeolite exhibited maximum compressive loads exceeding 25 N, attributable to the predominance of the continuous geopolymer matrix phase. As zeolite loading increased to 60 wt% or higher, compressive strength declined substantially due to insufficient binder content for effective particle-to-particle cohesion, resulting in mechanically fragile structures. The 50:50 zeolite-to-geopolymer ratio represents an optimal compromise, achieving compressive strengths of approximately 10 to 15 N sufficient for handling and fixed-bed reactor applications while maximizing adsorbent loading for CO_2 capture efficiency. This formulation provides adequate mechanical durability for industrial implementation without significantly diluting the active zeolite phase.

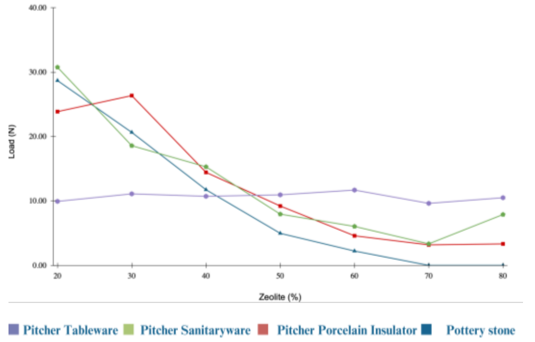

Figure 5. Single pellet crushing strength of Zeolite 13X/Geopolymer composites at varying zeolite ratios.

Carbon Dioxide Adsorption Performance of Pellets

To evaluate final material performance, pellets prepared at the 50:50 ratio were subjected to specific surface area analysis and CO_2 adsorption testing. Results demonstrate that pellets derived from pottery stone and sanitaryware retained the highest CO_2 adsorption capacity, Pellets tested at 25°C, 1 bar achieving 2.45 and 2.37 mmol/g respectively, equivalent to 10.78 and 10.43 wt% (**Table 2**). These adsorption capacities are competitive with literature-reported values for Zeolite 13X [1][2][8]. This superior performance correlates directly with retained high surface areas following pelletization at 415.36 and 398.64 m²/g respectively. These findings confirm that geopolymer-based pelletization does not significantly compromise zeolite efficiency, reinforcing the potential of sanitaryware waste as a viable precursor for producing effective CO_2 adsorbent materials. The adsorption capacities achieved are competitive with literature-reported values for Zeolite 13X pellets prepared using conventional binder systems.

Table 2 BET surface area and CO_2 adsorption performance CO_2 adsorption at 25°C/1 bar of pelletized Zeolite 13X (50:50 zeolite:geopolymer)

Sample	BET of Zeolite 13X pellet(m^2/g)	CO_2 absorb (mmol/g)	CO_2 Uptake (wt%)
Pottery Stone	415.36	2.45	10.78
Pitcher Porcelain Insulator	351.28	1.37	7.63
Pitcher Sanitaryware	398.64	2.37	10.43
Pitcher Tableware	356.29	1.54	8.38

CO_2 adsorption at 25°C, 1 bar. Capacity decreases ~30% at 100°C, ~60% at 200°C due to exothermic physisorption

Conclusion

This investigation successfully demonstrated the synthesis of Zeolite 13X from four distinct types of ceramic waste materials, namely pottery stone, pitcher porcelain insulators, pitcher porcelain tableware, and pitcher sanitaryware, through alkaline fusion at 800 °C followed by hydrothermal crystallization at 90 °C for 24 hours. X-ray diffraction analysis confirmed the formation of crystalline zeolite with characteristic FAU-type framework peaks at 2-theta approximately 6.2 degrees in all samples. Among the investigated raw materials, pitcher porcelain sanitaryware waste demonstrated the highest potential as a zeolite precursor, producing zeolite with superior crystallinity, sharp and intense diffraction peaks, and the highest specific surface area of 521.03 square meters per gram. Scanning electron microscopy analysis revealed that the synthesized zeolite crystals exhibited well-ordered polyhedral morphology characteristic of Zeolite 13X, with uniform particle distribution and absence of amorphous phases, confirming the effectiveness of the synthesis process.

Zeolite powder was successfully formed into 10-millimeter diameter spherical pellets using a metakaolin-based geopolymer binder. The optimal formulation ratio of zeolite to geopolymer at 50:50 by weight achieved the best balance between mechanical strength and adsorbent content, yielding compressive strengths of approximately 10 to 15 Newtons sufficient for handling and fixed-bed reactor applications. Geopolymer-based pelletization did not significantly compromise carbon dioxide adsorption performance. Pellets derived from sanitaryware waste retained a specific surface area of 398.64 square meters per gram and achieved a carbon dioxide adsorption capacity of 2.37 millimole per gram, equivalent to 10.43 weight percent, demonstrating excellent adsorbent properties suitable for industrial applications. These adsorption capacities are competitive with commercially available Zeolite 13X products, confirming the viability of ceramic waste as an effective precursor material.

The comprehensive findings establish that ceramic sanitaryware waste represents the most promising feedstock for synthesizing Zeolite 13X with efficient carbon dioxide capture capabilities. This research presents a sustainable, cost-effective, and industrially scalable method for converting non-biodegradable ceramic waste into high-value adsorbent materials, thereby supporting circular economy principles while addressing both waste management challenges and climate change mitigation. The proposed approach offers significant environmental benefits by simultaneously reducing landfill burdens and providing effective materials for greenhouse gas capture, with potential for implementation at both community and industrial scales.

Acknowledgements

The authors gratefully acknowledge the Department of Materials Science, Faculty of Science, Chulalongkorn University for providing research facilities and analytical equipment.

References

1. V. Garshasbi, M. Jahangiri, M. Anbia, Equilibrium CO_2 adsorption on zeolite 13X prepared from natural clays, Appl. Surf. Sci., Vol. 393, 225-233 (2017).
2. K.B. Jivrakh, et al., 3D-printed zeolite 13X gyroid monolith adsorbents for CO_2 capture, *Chem. Eng. J.*, Vol. 497, 154674 (2024)
3. H. Jedli, et al., Adsorption of CO_2, CH_4 and H_2 onto zeolite 13X: Kinetic and equilibrium studies, Heliyon, Vol. 10, e40672 (2024).
4. F. Rouquerol, J. Rouquerol, K. Sing, Adsorption by Powders and Porous Solids, Academic Press, London, 355-399 (1999).
5. C. Chen, D.-W. Park, W.-S. Ahn, CO_2 capture using zeolite 13X prepared from bentonite, Appl. Surf. Sci., Vol. 292, 63-67 (2014).
6. O. Stojkić, R.F., M. Janković, M. Perušić, D. Kostić, V.D. Srećko Stopić, Influence of process parameters on the adsorption properties of zeolite 13X, J. Chem. Technol. Environ., Vol. 5, 20-31 (2024).
7. L.S. Mohd Nazir, Y.F. Yeong, T.L. Chew, Methods and synthesis parameters affecting the formation of FAU type zeolite membrane and its separation performance: a review, J. Asian Ceram. Soc., Vol. 8, 1-19 (2020).
8. D.G. Boer, J. Langerak, P.P. Pescarmona, Zeolites as Selective Adsorbents for CO_2 Separation, ACS Appl. Energy Mater., Vol. 6, 2634-2656 (2023).

Synthesis of MnO_2 and MnO_2/C Composites from Spent Zn–C Batteries Using Hydrothermal Process

Apinya Suwaphapphattharaphon [1], **Pakinee Thongrit**[2], **Auscha Thongsri**[1], **Rojana Pornprasertsuk**[1,3,4,5]*
[1]Department of Materials Science, Faculty of Science, Chulalongkorn University, Thailand
[2]Synchrotron Light Research Institute, Thailand
[3]Center of Excellence in Petrochemical and Materials Technology, Chulalongkorn University, Thailand
[4]Center of Excellence on Advanced Materials for Energy Storage, Chulalongkorn University, Thailand
[5]Department of Materials Science and Bioengineering, Nagaoka University of Technology, Japan
*Corresponding author e-mail address rojana.p@chula.ac.th

Abstract

The growing volume of spent batteries, particularly Zn–C batteries, has become a significant contributor to electronic waste. The electrode powder from these batteries contains valuable materials such as zinc, manganese, and carbon that can be recovered and reused. This study focuses on recycling manganese and carbon to synthesize MnO_2 and MnO_2/C composite materials for use in new battery production. A literature review reveals that hydrothermal synthesis for recycling spent alkaline battery powder has been reported using two main approaches: (1) a two-step recycling process involving acid leaching followed by MnO_2 synthesis, and (2) a one-step recycling process in which MnO_2/C composites are directly synthesized without acid leaching. However, the one-step recycling process has not been previously applied to spent Zn–carbon battery powder. This work therefore investigates and compares the manganese recovery efficiency and material properties obtained from both methods when applied to Zn–C battery waste.

Keywords: Zn-C batteries; Manganese dioxide; Manganese recovery; Battery recycling; Hydrothermal synthesis

Background

The Zn-C battery is a primary cell widely used in common electronic devices such as radios, remote controls, and toys due to its low cost and ease of use. Its structure consists of a zinc (Zn) metal anode, which serves as the source of electrons, and a cathode made of manganese dioxide (MnO_2) mixed with carbon to enhance electrical conductivity. The electrolyte is typically an aqueous solution of ammonium chloride (NH_4Cl) or zinc chloride ($ZnCl_2$). During discharge, a redox reaction occurs between Zn and MnO_2. The main electrode reactions are as follows:

Anode: $Zn + 2Cl^- \rightarrow ZnCl_2 + 2e^-$

Cathode: $2MnO_2 + 2NH_4Cl + H_2O + 2e^- \rightarrow Mn_2O_3 + 2NH_4OH + 2Cl^-$

Overall reaction: $Zn + 2MnO_2 + 2NH_4Cl + H_2O \rightarrow ZnCl_2 + Mn_2O_3 + 2NH_4OH$

When $ZnCl_2$ is used as the electrolyte instead of NH_4Cl, the cathodic products may include Mn_3O_4 and $Zn(OH)_2$, depending on the cell chemistry after discharge. The anode undergoes oxidation to form ZnO, while the MnO_2 at the cathode is reduced to Mn_2O_3 or Mn_3O_4, and in some cases, forms a composite phase of $ZnO\cdot Mn_2O_3$. A study by Hasegawa *et al.* (2015) using X-ray diffraction (XRD) and scanning electron microscopy (SEM) revealed that spent Zn-C batteries contain ZnO, Mn_2O_3, Mn_3O_4, $ZnO\cdot Mn_2O_3$, and carbon. [1]

K. Manowilaikun [2] investigated the leaching behavior of manganese from the cathode powder of spent alkaline batteries using sulfuric acid at concentrations between 0.5–1.5 M, combined with 6% (v/v) hydrogen peroxide under ambient conditions for leaching times ranging from 15 to 180 minutes. After filtration to remove carbon residue, the resulting manganese sulfate solution was used to synthesize α-, β-, and γ-MnO_2 phases with a hydrothermal process, following synthesis conditions reported by Liu *et al.* [3] and Wang *et al.* [4], as summarized in Table 1. The results indicated that the obtained MnO_2 exhibited nanoscale particle sizes and high purity, with maximum manganese recovery rates of 87%, 64%, and 59% for the α-, β-, and γ-phases, respectively.

C. Waikhani [5] studied the leaching of manganese from spent alkaline and Zn-C batteries using sulfuric acid in combination with reducing agents such as hydrogen peroxide and sodium sulfide through a hydrothermal process. The manganese leaching efficiency (LE) was found to be highest at 78% for alkaline batteries and 88% for Zn-C batteries, respectively.

A. Thongsri [6] developed MnO_2/C composite materials derived from spent alkaline batteries using a one-step hydrothermal synthesis process to minimize acid consumption. The precursor used was untreated alkaline battery powder, which underwent hydrothermal synthesis to form MnO_2/C composites.The experimental results showed manganese recovery rates of 72.34%, 68.75%, and 61.9% for α, β, and γ-MnO_2/C composite, respectively

This research focuses on synthesizing MnO_2 and MnO_2/C composites from spent Zn-C battery powder with hydrothermal process, including both two-step and one-step recycling processes. The effects of precursors and synthesis temperature on the resulting phase composition and microstructure are investigated. The prepared materials are then employed as ZIB cathodes, and their electrochemical performance is compared between MnO_2 obtained from the two-step recycling process and MnO_2/C composites derived from the one-step recycling process.

Materials and Methods

Preparation of Electrode Powder from Spent Zn-C Batteries

Spent Zn-C batteries (AA size, Panasonic) were disassembled, and the electrode powder was collected and dried at room temperature for 24 hours. The dried powder was then ground using a vibratory mill and sieved through a 200-mesh screen (75 µm).

Synthesis of MnO_2 using Two-Step Recycling Process

A 5 g sample of the electrode powder was leached using 25 mL of 2 M sulfuric acid (H_2SO_4, QRëC) and 3 mL of 30% hydrogen peroxide (H_2O_2, QRëC). Subsequently, 6 mL of the leachate was mixed with 1.826 g of ammonium persulfate ($(NH_4)_2S_2O_8$, Kemaus) with and without 1.982 g of ammonium sulfate ($(NH_4)_2SO_4$, Kemaus) in deionized (DI) water. The total volume was adjusted to 35 mL with DI water, and the mixture was stirred for 15 min at room temperature. The solution was then transferred into a Teflon-lined stainless-steel autoclave and subjected to hydrothermal treatment at the temperatures specified in Table 1 for 24 hours. After the reaction, the products were washed with 500 mL of DI water followed by 250 mL of ethanol and subsequently dried at 60 °C for 24 hours.

Synthesis of MnO_2/C using One-Step Recycling Process

A 1.141 g sample of the electrode powder was mixed with 1.826 g of $(NH_4)_2S_2O_8$ with and without 1.982 g of $(NH_4)_2SO_4$. Either DI water or sulfuric acid (0.125 0.25 0.5 M). were used as the solvent. The acid concentration was systematically varied to investigate phase formation and to determine whether a pure-phase structure could be achieved under different acidic conditions. The resulting solution was then adjusted to a total volume of 35 mL.The mixture was stirred for 15 min at room temperature, then transferred into a Teflon-lined stainless-steel autoclave and subjected to hydrothermal treatment at the temperatures specified in Table 2 for 24 hours. After the reaction,

Table 1 Conditions for the synthesis of MnO_2 using two-step recycling process.

Phase	Reactants			Stirring time (min)	Temperature (°C)	Time (h)
	Leaching solution (mL)	$(NH_4)_2S_2O_8$ (mol)	$(NH_4)_2SO_4$ (mol)			
α-MnO_2	6	1.826	1.982	15	140	24
β-MnO_2	6	1.826	–	15	140	24
γ-MnO_2	6	1.826		15	90	24

Table 2 Conditions for the synthesis of MnO_2/C using one-step recycling process

Phase	Reactants			Stirring time (min)	Temperature (°C)	Time (h)
	Spent electrode powder (g)	$(NH_4)_2S_2O_8$ (mol)	$(NH_4)_2SO_4$ (mol)			
α-MnO_2/C	1.141	1.826	1.982	15	140	24
β-MnO_2/C	1.141	1.826	–	15	140	24
γ-MnO_2/C	1.141	1.826		15	90	24

the products were washed with 500 mL of DI water followed by 250 mL of ethanol and subsequently dried at 60 °C for 24 hours

Characterization

The microstructure, phase composition, and chemical constituents of the electrode powder were characterized using scanning electron microscopy (SEM), X-ray diffraction (XRD), and X-ray fluorescence spectroscopy (XRF), respectively.

Results and Discussion

MnO_2 using Two-Step Recycling Process

In earlier work, K. Manowilaikun et al. [2] (Table 3) demonstrated a maximum leaching efficiency of 87% through a two-step synthesis route for the recycling of alkaline batteries, yielding a single-phase product. Likewise, C. Waikhani et al. [5] examined the leaching characteristics of spent alkaline and Zn–C batteries, reporting a superior leaching efficiency of 88% for Zn–C batteries relative to alkaline counterparts. In contrast, the present study attained a markedly enhanced leaching efficiency of up to 98%, despite a substantial reduction in the amount of hydrogen peroxide (H_2O_2) employed as the reducing agent from 6 mL to 3 mL. While the mechanistic basis for this improvement cannot be conclusively determined from the available data, the findings indicate that, under the specified experimental conditions, high leaching performance can be sustained even at a reduced H_2O_2 dosage.

MnO_2 was synthesized through a two-step recycling process. The synthesis was designed to selectively produce α-MnO_2, β-MnO_2, and γ-MnO_2 phases. The XRD results, as shown in Figure 1, confirmed that each synthesis condition yielded a predominant single phase corresponding to the intended

Table 3 Synthesis of α-, β-, and γ-MnO_2 by two-step hydrothermal process conditions of alkaline from K. Manowilaikun [2]

Phase	Reactants			Stirring time (min)	Temperature (°C)	Time (h)	Reference
	Leaching solution	$(NH_4)_2S_2O_8$ (mol)	$(NH_4)_2SO_4$ (mol)				
α-MnO_2	Leaching solution 20 mL	0.008	0.015	Stir until homogeneous	140	12	[3,4]
β-MnO_2		0.008	-		140		
γ-MnO_2		0.008	-		80/90	4/12	
α-MnO_2	Leaching solution 20 mL	0.008	0.015		140	24	[5]
β-MnO_2		0.008	-		140	24	
γ^{α}-MnO_2		0.008	-		90	24	

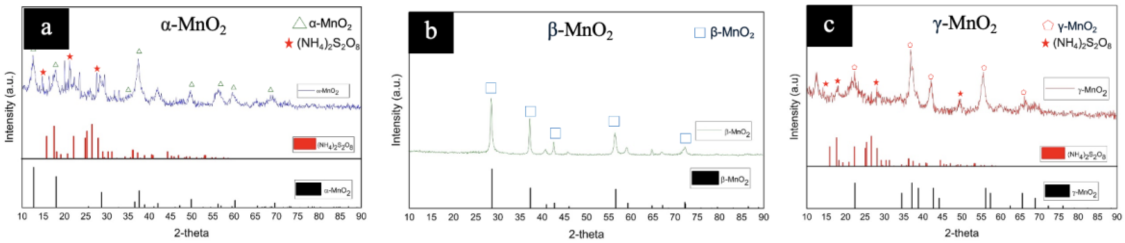

Figure 1 XRD patterns of MnO_2 from two-Step recycling process a) α-MnO_2, b) β-MnO_2 and c) γ-MnO_2.

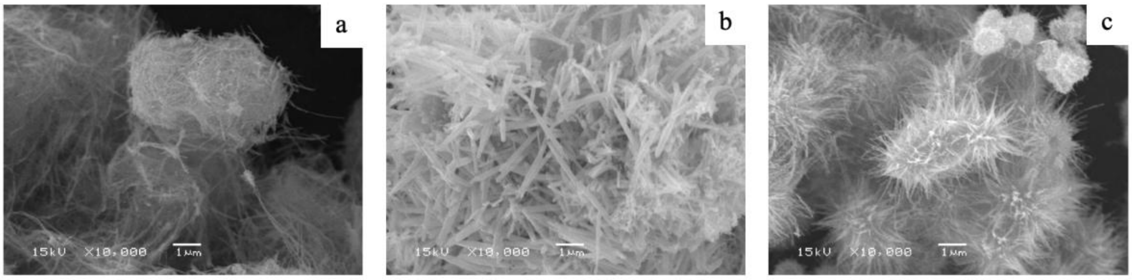

Figure 2 SEM images of MnO_2 from two-Step recycling process. a) α-MnO_2, b) β-MnO_2 and c) γ-MnO_2 at 10,000x magnification.

polymorph. However, minor peaks corresponding to ammonium persulfate were occasionally detected, which were presumed to originate from residual oxidizing agents remaining from the synthesis process.

The microstructural analysis performed using SEM, as shown in Figure 2, revealed that the α-MnO_2 phase exhibited well-aligned nanowire-like structures. In contrast, the β-MnO_2 phase presented nanorod-like morphologies that were shorter and thicker, whereas the γ-MnO_2 phase showed a nano-urchin-like architecture composed of radially assembled nanocrystals.

These distinct morphological characteristics of each MnO_2 phase are consistent with the observations reported in the previous study by K. Manowilaikun [2], which compared synthesized MnO_2 samples with commercial MnO_2. The synthesized materials demonstrated morphological features like those of their commercial counterparts within each polymorph. Such morphology-dependent differences are noteworthy, as they are expected to influence the electrochemical behavior and potential applications of these materials in energy-related systems.

MnO_2/C using One-Step Recycling Process

Previous work by A. Thongsri [6], Table 4 which employed a one-step synthesis process for recycling alkaline batteries, reported Mn recovery efficiency of 72.34%, yielding products consisting of both single-phase and mixed-phase structures. Building upon this study, the present work investigates a non-acid synthesis route as well as acid-assisted processes using acid concentrations of 0.125, 0.25, and 0.5 M. The results indicate that the highest manganese recovery of approximately 45.15% was achieved under acid-free conditions. The relatively lower recovery efficiency may be attributed to differences in battery types, which could limit the extent of Mn recovery. Nevertheless, the proposed recovery process significantly reduces chemical

Table 4 Synthesis of α-, β-, and γ-MnO_2/C by one-step hydrothermal process conditions of alkaline from A. Thongsri [6]

Phase	Reactants			Stirring time (min)	Temperature (°C)	Time (h)	Reference
	Spent electrode powder (g)	$(NH_4)_2S_2O_8$ (mol)	$(NH_4)_2SO_4$ (mol)				
α-MnO_2/C	1	0.008	0.015	15	140	24	[6]
β-MnO_2/C	1	0.008	-	15	140	24	
γ-MnO_2/C	1	0.008		15	90	24	

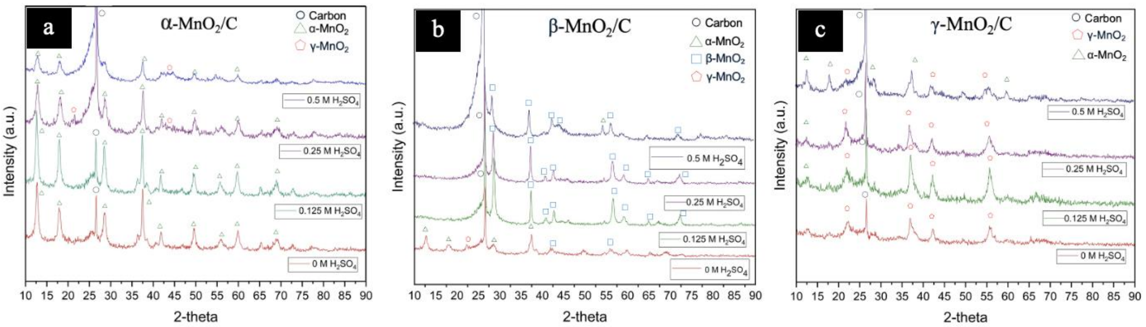

Figure 3 XRD patterns of MnO_2/C from one-step recycling process a) α-MnO_2/C, b) β-MnO_2/C and c) γ-MnO_2/C.

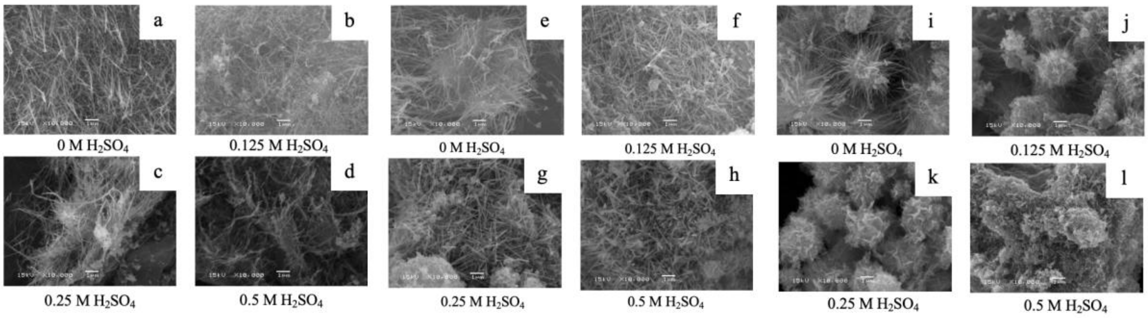

0 M H_2SO_4 0.125 M H_2SO_4 0 M H_2SO_4 0.125 M H_2SO_4 0 M H_2SO_4 0.125 M H_2SO_4

0.25 M H_2SO_4 0.5 M H_2SO_4 0.25 M H_2SO_4 0.5 M H_2SO_4 0.25 M H_2SO_4 0.5 M H_2SO_4

Figure 4 SEM images of MnO_2/C from one-step recycling process. a) α-MnO_2/C 0 M H_2SO_4 b) α-MnO_2/C 0.125 M H_2SO_4 c) α-MnO_2/C 0.25 M H_2SO_4 d) α-MnO_2/C 0.5 M H_2SO_4 e) β -MnO_2/C 0 M H_2SO_4 f) β -MnO_2/C 0.125 M H_2SO_4 g) β -MnO_2/C 0.25 M H_2SO_4 h) β -MnO_2/C 0.25 M H_2SO_4 i) γ-MnO_2/C 0 M H_2SO_4 j) γ-MnO_2/C 0.125 M H_2SO_4 k) γ-MnO_2/C 0.25 M H_2SO_4 and l) γ-MnO_2/C 0.5 M H_2SO_4 at 10,000x magnification.

consumption and overall cost compared to the conventional two-step synthesis approach.

Manganese dioxide/carbon (MnO_2/C) composites were synthesized through a one-step recycling process using different acid concentrations, including non-acidic, 0.125 M, 0.25 M, and 0.5 M conditions. The synthesis was designed to obtain α-MnO_2/C, β-MnO_2/C, and γ-MnO_2/C phases, respectively. XRD patterns, as shown in Figure 3, confirmed that the synthesized products primarily consisted of α-MnO_2 as the dominant phase along with carbon. The presence of carbon resulted from the use of Zn–C battery powder, which inherently contains carbon as a component in the precursor material.

For the α-MnO_2/C synthesis, the samples prepared under non-acid, and 0.125 M acid conditions exhibited α-MnO_2 and carbon as the major phases. In contrast, the samples synthesized at 0.25 M and 0.5 M acid concentrations yielded α-MnO_2 and carbon as the dominant phases with minor γ-MnO_2 peaks detected, suggesting that α-MnO_2 tends to form and grow preferentially under mildly acidic conditions.

In the β-MnO_2/C synthesis, products obtained from 0.125 M, 0.25 M, and 0.5 M acid concentrations predominantly exhibited β-MnO_2 and carbon phases. However, under the non-acidic condition, mixed phases of α-, β-, and γ-MnO_2 were observed. This result indicates that the absence of acid during synthesis may lead to less-controlled crystallization, resulting in the coexistence of multiple MnO_2 polymorphs.

For the γ-MnO_2/C synthesis, the non-acidic condition produced γ-MnO_2 and carbon as the main phases. When acid concentrations of 0.125 M, 0.25 M, and 0.5 M were applied, β-MnO_2 and carbon became the dominant phases, with α-MnO_2 appearing as a minor phase. These findings suggest that γ-MnO_2 is more likely to form and stabilize under low-acid conditions. A small amount of ammonium persulfate residue was detected in certain samples, which is presumed to have originated from residual oxidizing agents remaining after the washing process.

The microstructure of the synthesized manganese dioxide–carbon (MnO_2/C) composites was examined using SEM , as shown in Figure 4. Distinct morphological differences were observed depending on the crystal phase of the material. For the α-MnO_2/C phase, the structure predominantly consisted of nanowires forming well-aligned, elongated networks. In contrast, the β-MnO_2/C phase also exhibited a nanorod-like morphology; however, these nanorods were shorter and thicker compared to the nanowires of the α phase. The γ-MnO_2/C phase displayed a nano-urchin-like morphology, characterized by the aggregation of numerous nanoscale crystallites into a spherical, branched architecture. Additionally, spherical particles, likely corresponding to acetylene black carbon, were observed dispersed within the composite matrix.

It is noteworthy that the α phase was primarily obtained under acid-free synthesis conditions, whereas the β phase formed at acid concentrations of 0.125, 0.25, and 0.5 M. The γ phase was predominantly observed under acid-free conditions. SEM analysis indicates that these synthesis conditions allow the formation of the desired primary phase along with carbon as a major component, with minimal presence of secondary phases.

The distinct morphologies of the α, β, and γ phases are consistent with their respective crystal structures and the specific synthesis conditions employed. Differences in nanostructure, such as the nanowires of α-MnO_2 and the nano-urchins of γ-MnO_2, are expected to influence the electrochemical properties and potential applications of these materials. Overall, this study demonstrates the effectiveness of the one-step recycling process in controlling both the crystal phase composition and microstructural features of MnO_2/C composite materials.

In future work, this study will evaluate the specific capacity and cycling performance of MnO_2 and MnO_2/C composites to compare their electrochemical performance with the results summarized in Table 5.

Table 5 Specific capacity and cycling performance of MnO_2 and MnO_2/C composite of cathode for Zn-ion battery

Cathode	Voltage (V)	Specific capacity (mAh/g)	Electrolyte	Cycling performance	Reference
α-MnO_2	0.8 -1.9	264 at 0.3 C	2 M $ZnSO_4$	83.5% at 6000 cycles	[9]
β-MnO_2	1.0 - 1.8	~104 at 0.1 A/g	1 M $ZnSO_4$ + 0.1 M $MnSO_4$	99% at 100 cycles	[10]
γ-MnO_2	1.0 - 1.8	285 at 0.5 mA/cm	1 M $ZnSO_4$	~100% at 40 cycles	[7]
α-MnO_2	1.0 - 1.8	113 at 0.1 A/g	2 M $ZnSO_4$	51.2% at 1000 cycle	[8]
α-MnO_2/C		230 at 0.1 A/g		80.8% at 1000 cycles	
α-MnO_2/C	1.0-1.75	250 at 0.12 A/g	2 M $ZnSO_4$	~48% at 300 cycles	[6]
β-MnO_2/C		375 at 0.12 A/g		~30% at 300 รอบ	
γ-MnO_2/C		300 at 0.12 A/g		~42% at 300 cycles	

Conclusion

MnO_2 and MnO_2/C materials synthesized through recycling processes exhibit controllable crystal phases and nanostructures. The two-step recycling process selectively produces α-, β-, and γ-MnO_2 phases with distinct morphologies including nanowire, nanorod, and nano-urchin structures, while the one-step recycling process simultaneously recovers manganese and carbon, enabling control over both phase composition and structural characteristics. Acid concentration plays a crucial role in phase formation: α-MnO_2/C predominantly forms under low or non-acidic conditions, β-MnO_2/C at acid concentrations of 0.125–0.5 M, and γ-MnO_2/C primarily under non-acidic conditions. The resulting nanostructures and carbon distribution are expected to significantly influence the electrochemical properties and potential applications of these recycled materials in energy storage systems.

Acknowledgement

The authors would like to acknowledge the scholarship support for Ms. Apinya Suwaphapphattharaphon from the Wittayabundit Scholarship, Faculty of Science, Chulalongkorn University. This project was funded by the Center of Excellence on Advanced Materials for Energy Storage, Faculty of Science, Chulalongkorn University, and the National Research Council of Thailand (NRCT) under Grant Number N11A670659.

References

1. M. Hasegawa, R. Ueyama, Y. Kashiwaya, and T. Hirato, "Recovery of Zinc from Used Alkali Manganese Dry Cells," *J. Sustain. Metall.*, vol. 1, no. 2, pp. 144–150, (2015).
2. K. Manowilaikun, "Synthesis of manganese dioxide from spent alkaline batteries for zinc-ion battery and Supercapacitor applications," Master of Science Thesis,(2020).
3. Y. Liu, J. Wei, Y. Tian, and S. Yan, "The structure–property relationship of manganese oxides: Highly efficient removal of methyl orange from aqueous solution," *J. Mater. Chem. A*, vol. 3, no. 37, pp. 19000–19010, (2015).
4. X. Wang and Y. Li, "Synthesis and formation mechanism of manganese dioxide nanowires/nanorods," *Chem. Eur. J.*, vol. 9, no. 1, pp. 300–306, (2002).
5. C. Waikhani, "Synthesis of manganese dioxide from spent zinc carbon and alkaline Batteries for zinc-ion battery application" Master of Science Thesis, (2021).
6. A. Thongsri, "Synthesis of MnO_2/C Composite from Spent Alkaline Battery by One-Step Hydrothermal Process for Rechargeable Zn-Ion Battery Application," Master of Science Thesis, (2023).
7. X. Wang and Y. Li, "Synthesis and formation mechanism of manganese dioxide nanowires/nanorods," *Chem. Eur. J.*, vol. 9, no. 1, pp. 300–306, (2002).
8. M. H. Alfaruqi et al., "Electrochemically induced structural transformation in a γ-MnO_2 cathode of a high-capacity zinc-ion battery system," *Chem. Mater.*, vol. 27, no. 10, pp. 3609–3620, (2015).
9. J. Cao et al., "Mechanochemical reactions of MnO_2 and graphite nanosheets as a durable zinc ion battery cathode," *Appl. Surf. Sci.*, vol. 534, p. 147630, (2020).
10. K. Ma, Q. Li, C. Hong, G. Yang, and C. Wang, "Bi doping-enhanced reversible-phase transition of α-MnO_2 raising the cycle capability of aqueous Zn–Mn Batteries," *ACS Appl. Mater. Interfaces*, vol. 13, no. 46, pp. 55208–55217, (2021).
11. C. Guo et al., "A case study of β- and δ-MnO_2 with different crystallographic forms on ion-storage in rechargeable aqueous zinc ion battery," *Electrochim. Acta*, vol. 324, p. 134867, (2019).

Investigation of Potential Interaction and Oxide Dispersion in Cesium Dihydrogen Phosphate – Titanium Dioxide Composites Prepared via various Methods

Sunithi Ratana[2], Apirat Theerapapvisetpong [1, 2] and Chatr Panithipongwut Kowalski [1, 2, *]
[1] Upcycled Materials from Industrial and Agricultural Wastes Research Unit, Department of Materials Science, Faculty of Science, Chulalongkorn University, Phyathai Road, Bangkok, 10330
[2] Department of Materials Science, Faculty of Science, Chulalongkorn University, Bangkok, 10330, Thailand
*Corresponding author e-mail address: chatr.p@chula.ac.th

Abstract

Cesium dihydrogen phosphate has been widely studied as an electrolyte for intermediate-temperature fuel cells due to its high proton conductivity and its potential. Previous research has shown that oxide additives can enhance the stability and performance of cesium dihydrogen phosphate. However, it remains unclear whether interactions with oxide additives induce structural changes or lead to the formation of new compounds. Clarifying this issue is important because combining cesium dihydrogen phosphate with oxides may influence both stability and microstructural properties, thereby affecting its potential application as a composite electrolyte. This work aims to investigate whether interactions or new phases form between cesium dihydrogen phosphate and titanium dioxide prepared by three different methods: coprecipitation, mechanical grinding, and a combined method. X-ray diffraction (XRD) was used to identify crystalline phases and detect any new compounds. While Raman spectroscopy and Fourier-transform infrared spectroscopy (FTIR) were employed to identify possible bonding between cesium dihydrogen phosphate and titanium dioxide. Scanning electron microscopy (SEM) with energy-dispersive spectroscopy (EDS) was employed to observe particle morphology and dispersion of titanium dioxide within the composites. Comparison of the three synthesis methods reveals how preparation methods influence mixing quality, interfacial contact, and the possibility of new phase formation. The findings will help clarify how cesium dihydrogen phosphate and titanium dioxide interact and provide useful guidance for preparing composite electrolyte materials.

Keywords: Cesium dihydrogen phosphate, Titanium dioxide, synthesis methods

---

Background

The growing demand for alternative energy has made fuel cells a promising technology, mainly due to concerns about petroleum depletion and pollution from internal combustion engines. According to Mekhilef et al. [1], diesel engines operate with efficiencies up to only 35%, whereas fuel cells can reach 40-85%. Solid acids have gained attention as electrolytes for intermediate temperature fuel cells because they exhibit properties between acids and salts. They can release protons (H^+) like acids while remaining brittle and electrically insulating like salts. When heated to appropriate temperatures, solid acids undergo a superprotonic phase transition that greatly increases its proton conductivity. However, the material softens and loses mechanical strength at elevated temperatures, leading to structural deformation under compressive stress from electrodes and gas channels during operation. To address this issue, Mikhail et al. [2] demonstrated that incorporating silicon dioxide (SiO_2) into $CsHSO_4$ improved its thermomechanical strength by filling grain boundaries and limiting grain movement. This concept became a useful approach for improving the strength of solid acid electrolytes by using oxide additives. According to the CRC Materials Science and Engineering Handbook [3], Titanium dioxide (TiO_2) possesses a much higher Young's modulus (~282 GPa) than SiO_2 (~73 GPa), indicating greater stiffness. These characteristics make TiO_2 a promising additive for reinforcing CsH_2PO_4. Previous studies [4-7] indicated that the ratio between solid acids and inert oxides strongly affect the conductivity of composite electrolytes. Leonova et al. [4] found that a certain content of inert oxide can improve electrical properties, whereas excessive loading reduces proton transport by limiting percolation pathways. Hence, a 7:3 molar ratio was adopted in this work to achieve effective reinforcement with minimal influence on conductivity. However, this study focuses on synthesizing CsH_2PO_4/TiO_2 composites using three different preparation methods: coprecipitation, mechanical grinding, and a combined approach to compare the effectiveness of each synthesis method. X-ray diffraction (XRD) was employed to identify possible new phases, while Raman Spectroscopy and Fourier transform infrared (FTIR) spectroscopy were used to detect vibrational features that may indicate bonding or interaction. Scanning electron microscopy with energy-dispersive spectroscopy (SEM/EDS) was used to observe particle morphology and TiO_2 distribution within the CsH_2PO_4 matrix. Comparing the three synthesis methods provides insight into how preparation conditions affect mixing quality, interfacial contact, and phase stability, offering guidance for developing durable CsH_2PO_4 based composite electrolytes for intermediate-temperature fuel cells.

Materials and Methods

Sample preparation

Preparation of CsH_2PO_4/TiO_2 Composites via Different Methods

1. Mechanical Grinding Method
CsH_2PO_4/TiO_2 composites were prepared by mixing CsH_2PO_4 with TiO_2 in a 7:3 molar ratio. The mixture was ground using an agate mortar for 15 minutes to obtain a uniform mixture of the powders.

2. Coprecipitation Method
CsH_2PO_4/TiO_2 composites were synthesized via the coprecipitation method, with a fixed molar ratio of 7:3 between CsH_2PO_4 and TiO_2. First, Cs_2CO_3 was dissolved in water, followed by the gradual addition of H_3PO_4. The required amount of inert oxide was then added, followed by stirring with a magnetic stirrer for 15 minutes. Methanol was subsequently added to induce precipitation. The obtained crystals were then dried at 90 °C for 24 hours.

3. Coprecipitation Combined with Mechanical Grinding
The coprecipitation procedure was performed as previously described. The dried product was subsequently ground with an agate mortar for 15 minutes to improve homogeneity.

Characterization

X-ray Diffraction (XRD)

The crystal structure of the samples was examined using X-ray diffraction (XRD) with a Panalytical Aeris Benchtop DY741diffractometer equipped with a Cu Kα radiation source operated at a voltage of 40 kV and a current of 15 mA. Data were collected over a 2θ range of 10°-70° with a step size of 0.02° and a scan time of 1 second per step. The samples were prepared in powder form. The resulting patterns were used to identify crystalline phases and to evaluate how different synthesis methods influenced structural characteristics and potential phase formation.

Scanning Electron Microscopy (SEM) and Energy-Dispersive X-ray Spectroscopy (EDS)

The microstructures of CsH_2PO_4/TiO_2 composites synthesized by three different methods were examined using scanning electron microscopy (SEM), while the elemental distribution was analyzed by energy-dispersive X-ray spectroscopy (EDS). To minimize particle agglomeration, each powder sample was first dispersed in methanol and then dried at room temperature. The dried powders were mounted onto carbon tape and sputter-coated with a thin layer of gold. All observations were conducted using a JEOL JCM-7000 Benchtop Scanning Electron Microscope

Raman Spectroscopy

Raman spectroscopy was performed to analyze structural characteristics and detect the presence of TiO_2 in CsH_2PO_4-based composites synthesized by three different methods: mechanical grinding, coprecipitation, and the combined approach. The measurements were conducted on powder samples using an Xplora Plus Raman spectrometer (Horiba) with a 785 nm laser. A 50x objective lens was used, and spectral data were collected with an acquisition time of 1 second per point, using a 500 μm hole, a 200 μm slit, and a 600 lines/mm grating.

Fourier Transform Infrared Spectroscopy (FTIR)

Fourier transform infrared spectroscopy (FTIR) was performed to identify the functional groups and bonding characteristics of the samples. Powder samples were prepared using the KBr mode. Each sample was thoroughly mixed with spectroscopic-grade KBr and then pressed into a pellet using a hydraulic press. The spectra were recorded using a FTIR Spectrometer Thermo Scientific Nicolet iS50 in the wavenumber range of 400-4500 cm^{-1} in transmittance mode.

Results and discussions

X-ray Diffraction (XRD)

The XRD patterns of pure CsH_2PO_4 and TiO_2 composites synthesized via three different methods are shown in Figure 1. The pure CsH_2PO_4 sample exhibits characteristic diffraction peaks consistent with CsH_2PO_4, with prominent peaks observed around $2\theta \approx$ 18.2°,19.1° 23.7°, 25.4°, 27.9°, 29.0°, 34.1°, 35.0°, 36.9°, 37.8° and 48.5° For the composites containing TiO_2, additional diffraction peaks corresponding to the anatase phase of TiO_2 are detected in all three synthesis methods: mechanical grinding, coprecipitation, and the combined method. These peaks are observed at $2\theta \approx$ 25.3°, 37.8°, and 48.0°, with the most prominent peak at 25.3°, which agrees with the standard JCPDS card No. 00-021-1272 for anatase TiO_2. The presence of these peaks confirms that the TiO_2 phase remains stable after incorporation, indicating no significant interaction with the CsH_2PO_4 matrix.

Scanning Electron Microscopy (SEM) and Energy Dispersive X-ray Spectroscopy (EDS)

Figure 2 shows SEM micrographs and EDS elemental mapping images of Cs and Ti for CsH_2PO_4/TiO_2 composites prepared via several methods: coprecipitation, mechanical grinding, and a combined method. The SEM images at magnifications of x500 and x3000 reveal differences in surface morphology depending on the synthesis methods. EDS mapping results confirm the presence of Ti across all samples, indicating successful incorporation of TiO_2 in all composites. In samples prepared by coprecipitation, Ti signals are mostly located within the bulk of the CsH_2PO_4 matrix with minimal surface presence. In contrast, mechanical grinding leads to a broader distribution of Ti across the surface, with fine TiO_2 particles appearing to cover CsH_2PO_4 grains without significant agglomeration. In the sample prepared by the combined method, Ti was clearly distributed on the surface. However, some TiO_2 agglomeration was also observed.

Raman Spectroscopy

Figure 3 shows Raman spectroscopy was employed to investigate the vibrational characteristics of the samples. Pure CsH_2PO_4 exhibited distinct peaks below 300 cm^{-1}, which can be assigned to lattice modes related to Cs^+ and PO_4^{3-} groups, as well as broad bands in the 400-1300 cm^{-1} region corresponding to phosphate bending and stretching vibrations [8,9]. In the TiO_2 composites samples, additional peaks were observed in the range of 144, 195, 517, and 638 cm^{-1} [10], which are attributed to the anatase phase of TiO_2. These anatase peaks were clearly detected in all composites, indicating the presence of TiO_2 in the final materials regardless of synthesis method. This suggests that the TiO_2 fillers retained their crystallinity and remained separate from the CsH_2PO_4 matrix. The vibrational bands of CsH_2PO_4 remained mostly unchanged, implying that there was no significant chemical reaction between the matrix and the oxide fillers.

Fourier Transform Infrared Spectroscopy (FTIR)

The FTIR spectra of CsH_2PO_4 and its TiO_2 composites samples prepared via coprecipitation, mechanical grinding, and the combined method are shown in Figure 4. Several characteristic vibrational peaks were observed, corresponding to the molecular bonds in the CsH_2PO_4 matrix and TiO_2. The stretching vibrations of Cs-O and P-O bonds appeared in the range of 400-800 cm^{-1}, while stretching P-OH and bending P-O modes were detected around 800-1300 cm^{-1}. In particular, the PO_4^{3-} vibrational modes were identified at 930, 1080, 1100, and 1216 cm^{-1}, consistent with previous reports [11]. Importantly, additional peaks attributed to Ti-O-Ti bonds were observed within 500-700 cm^{-1} in all composite samples, confirming the presence of TiO_2. These features observed in the transmittance spectra did not exhibit any significant shifts or intensity changes that would suggest chemical interactions between the oxide filler and the matrix. This indicates that TiO_2 acted as an inert filler, preserving its structural integrity without disrupting the CsH_2PO_4 framework.

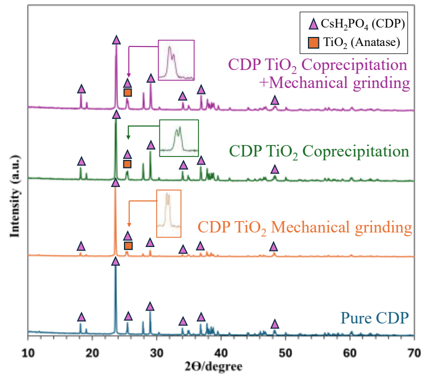

Figure 1 XRD patterns of CsH_2PO_4 and CsH_2PO_4/TiO_2 composites prepared via different synthesis methods.

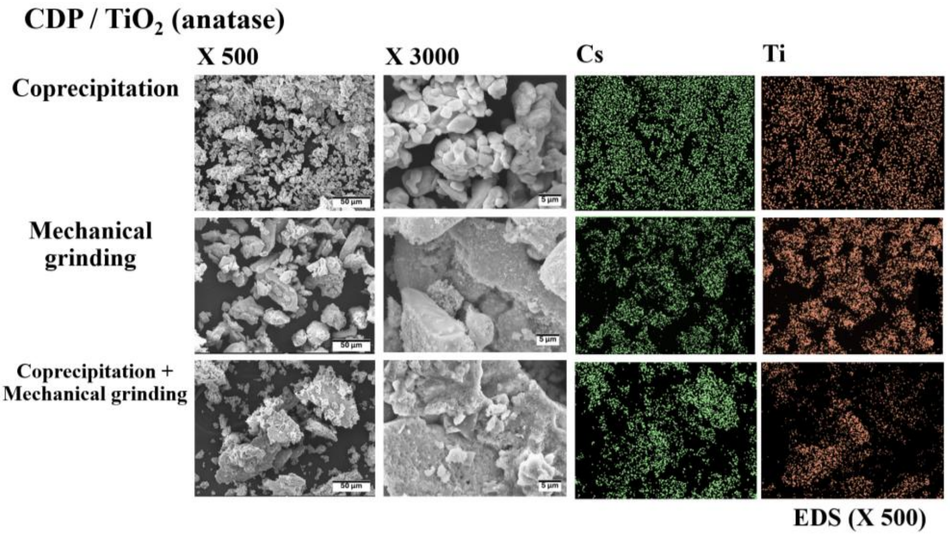

Figure 2 Surface morphology and elemental mapping of CsH_2PO_4/TiO_2 composites synthesized by different synthesis methods.

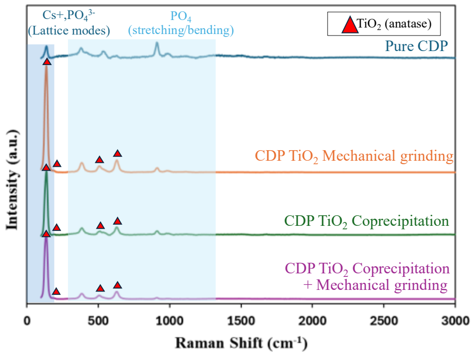

Figure 3 Raman spectra of pure CsH_2PO_4 and TiO_2 added composites prepared by different synthesis methods

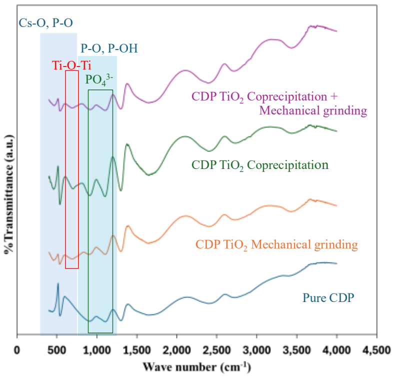

Figure 4 FTIR spectra of pure CsH_2PO_4 and CsH_2PO_4/TiO_2 composites prepared by different synthesis methods.

Conclusion

CsH_2PO_4/TiO_2 composites were prepared via different synthesis methods: coprecipitation, mechanical grinding, and a combined method. All samples exhibited similar structural characteristics with no evidence of new phase formation as confirmed by XRD, FTIR, and Raman analyses. SEM/EDS results revealed that TiO_2 particles were present in all samples; however, mechanical grinding achieved the most uniform dispersion without noticeable agglomeration. In contrast, the coprecipitation method led to TiO_2 being embedded within the CDP matrix, while the combined method showed partial clustering. Therefore, mechanical grinding appears to be the most effective method for preparing well-dispersed CDP/TiO_2 composites.

Acknowledgements

We would like to sincerely thank the Center of Excellence on Advanced Materials for Energy Storage and the Upcycled Materials from Industrial and Agricultural Wastes Research Unit, Faculty of Science, Chulalongkorn University, for their continued support throughout this work

References

1. S. Mekhilef, R. Saidur, A. Safari, *Comparative study of different fuel cell technologies*, *Renew. Sustain. Energy Rev.*, Vol. 16, 981-989 (2012).
2. M. N. Kislitsyn, *Materials Chemistry of Superprotonic Solid Acids*, PhD Thesis, California Institute of Technology, Pasadena, California (2009).
3. W. A. Shackelford, *CRC Materials Science and Engineering Handbook*, 3rd Edition, CRC Press, New York (2001).

4. L. S. Leonova, Y. A. Dobrovolsky, D. I. Domashnev, A. E. Ukshe, O. M. Grebtsova, I. V. Arkhangel'skii, *Peculiarities of electrochemical behavior of* $CsHSO_4$–SnO_2 *composite system*, *Russ. J. Electrochem.*, Vol.39, 495-500 (2003).
5. J. Otomo, H. Shigeoka, H. Nagamoto, H. Takahashi, *Phase transition behavior and proton conduction mechanism in cesium hydrogen sulfate/silica composite*, *J. Phys. Chem. Solids*, Vol. 66, 21-30 (2005).
6. J. Otomo, T. Ishigooka, T. Kitano, H. Takahashi, H. Nagamoto, *Phase transition and proton transport characteristics in* CsH_2PO_4/SiO_2 *composites*, *Electrochim. Acta*, Vol. 53, 8186-8195 (2008).
7. D. Singh, P. Kumar, J. Singh, D. Veer, A. Kumar, R.S. Katiyar, *Structural, thermal and electrical properties of composite electrolytes* $(1-x)$ $CsH_2PO_4/xZrO_2$ $(0 \leq x \leq 0.4)$ *for fuel cell with advanced electrode*, *SN Appl. Sci.*, Vol. 3, 227-236 (2021).
8. F. Romain, A. Novak, *Raman study of the high-temperature phase transition in* CsH_2PO_4, *J. Mol. Struct.*, Vol. 263, 69-74 (1991).
9. B. Marchon, A. Novak, Vibrational study of CsH_2PO_4 and CsD_2PO_4 single crystals, *J. Chem. Phys.*, Vol. 78, 2105-2120 (1981).
10. S.S. El-Deen, A.M. Hashem, A.E. Abdel Ghany, S. Indris, H. Ehrenberg, A. Mauger, C.M. Julien, *Anatase* TiO_2 *nanoparticles for lithium-ion batteries*, *Ionics*, Vol. 24, 2925-2934 (2018).
11. D. Singh, J. Singh, P. Kumar, D. Veer, D. Kumar, R.S. Katiyar, A. Kumar, A. Kumar, *The influence of* TiO_2 *on the proton conduction and thermal stability of* CsH_2PO_4 *composite electrolytes*, *S. Afr. J. Chem. Eng.*, Vol.37, 227-236 (2021).

Effect of synthesis parameters on crystallinity of zeolite 13X derived from porcelain insulator waste by alkali fusion method

K. Sinwanasarp [1,2], N. Nawaukkaratharnant [2,3], A. Theerapapvisetpong [1,2*]
[1] Department of Materials Science, Faculty of Science, Chulalongkorn University, Bangkok, 10330 Thailand
[2] Upcycled Materials from Industrial and Agricultural Wastes Research Unit, Department of Materials Science, Faculty of Science, Chulalongkorn University, Bangkok, 10330, Thailand
[3] Metallurgy and Materials Science Research Institute, Chulalongkorn University, Bangkok, 10330, Thailand
*Corresponding author e-mail address: apirat.t@chula.ac.th

Abstract

An increase in volume of discarded porcelain insulators has challenged environmentally due to their high durability, complex disposal process, and non-biodegradable nature. Traditional disposal methods, such as landfilling, are neither sustainable nor environmentally friendly. Since the porcelain insulators are primarily composed of silica and alumina, key components in zeolite formation, repurposing them into Zeolite 13X aligns with circular economy principles while addressing waste accumulation. In this research, zeolite 13X was synthesized from porcelain insulator waste using the alkaline fusion method without additional silica or alumina sources, and its ability to adsorb carbon dioxide was investigated. The synthesis parameters, including NaOH/porcelain insulator waste mass ratios (0.8:1.0 to 1.2:1.0), fusion temperatures (500-650°C for 2 h), pre-crystallization temperatures (room temp -70°C for 2 h), and crystallization temperatures (80-90°C for 24 h), were focused. The result indicates that the optimal NaOH/porcelain insulator waste mass ratio and fusion temperature, which can dissolve quartz and mullite of porcelain insulator waste, were 1.2:1 and 650°C, respectively. This study demonstrates that porcelain insulator waste can be successfully utilized as a raw material for zeolite 13X synthesis.

Keywords: Porcelain insulator waste; Zeolite 13X; Alkali fusion method; CO_2 adsorption

---

Background

Porcelain insulators are often utilized elements in electrical power distribution systems; nonetheless, they are susceptible to degradation from numerous environmental and operational conditions, including aging, cracking, and dielectric breakdown [1]. The increasing quantity of decommissioned and discarded porcelain insulators has become an environmental issue in management of this ceramic waste [2]. Most porcelain insulators are predominantly composed of aluminosilicate materials, which exhibit chemical stability and non-degradability. Inadequate disposal of these pollutants, along with excessive landfill buildup. Consequently, the recycling and valorization of waste porcelain have garnered increasing interest as a sustainable method for transforming industrial waste into value-added products.

A possible application for waste porcelain is its use as a precursor material in the manufacture of zeolite, especialy Zeolite 13X. Zeolite 13X is a crystalline aluminosilicate featuring a three-dimensional framework of interconnected SiO_4 and AlO_4 tetrahedra, which creates a porous network with significant cation-exchange capacity and adsorption potential. Zeolite 13X possesses distinctive structural attributes, resulting in a large surface area, consistent pore size distribution, and exceptional thermal and chemical resilience. The framework structure often comprises a supercage featuring a pore aperture of roughly 10 Å and an interior cavity diameter of around 13 Å, rendering it very efficient for adsorption and ion-exchange activities. Extensive surface area and adjustable chemical composition of zeolite 13X facilitate its use in gas adsorption, ion exchange, separation, and catalysis, including CO_2 capture, heavy metal extraction, and industrial gas purification [3-4].

A multitude of researchers has investigated the production of Zeolite 13X from diverse industrial and natural waste sources, seeking to substitute expensive pure chemicals like sodium silicate and sodium aluminate with sustainable alternatives. For example, fly ash, kaolin, and waste glass have been effectively employed as sources of silica and alumina [5-6]. Muhammad Yousuf et al. manufactured Zeolite 13X from waste glass and fly ash by alkali fusion and hydrothermal techniques[7], attaining elevated crystallinity and adsorption capacity [8-11]. Goujon Ke et al. represented the synthesis of zeolite X from fly ash via alkaline fusion and subsequent hydrothermal treatment, noting that temperature and NaOH ratio markedly affected phase purity and crystal shape. Takaki Wajima and colleagues produced Zeolite 13X from coal fly ash using NaOH fusion at 600 °C, followed by hydrothermal aging, yielding a high cation-exchange capacity and crystalline phase development [8-9].

The alkali fusion technique has demonstrated efficacy in transforming inert aluminosilicate waste into reactive phases appropriate for zeolite production. This procedure generally entails combining the waste precursor with NaOH in designated ratios (1:1–1.5 by weight) and subjecting the mixture to temperatures ranging from 550–750 °C for several hours to produce sodium aluminosilicate intermediates. The fused materials undergo hydrothermal treatment, typically at temperatures ranging from 90 to 150 °C for 6 to 24 hours, to promote crystallization into zeolite phases. The synthesis factors, such as the NaOH-to-waste ratio, fusion temperature, crystallization temperature, and duration, are critical in influencing the resultant zeolite type, purity, and yield [12].

The synthesis of Zeolite 13X is strongly governed by the chemical composition of the precursor and synthesis parameters, which determine both the zeolite type and product purity. As reported by Shuai Gao et al. [13], optimizing the Na_2O/SiO_2 and SiO_2/Al_2O_3 ratios during alkali fusion is critical for achieving high crystallinity and enhanced CO_2 adsorption, with a Si/Al ratio of approximately 1.23 providing the optimal framework charge balance and cation distribution for superior ion-exchange capacity. Similarly, Zhijuan Zhang et al. [14] demonstrated that crystallization temperature and NaOH concentration dictate the resulting phase: lower alkalinity and temperature favor Zeolite A (LTA type), while higher values promote the formation of Zeolite 13X (FAU type) with greater surface area and adsorption performance. Collectively, these findings highlight that precise control of Si/Al ratio, alkalinity, and thermal conditions is essential for obtaining phase-pure, highly crystalline FAU-type Zeolite 13X with optimized structural and adsorption properties.

The compositional resemblance of porcelain insulators, which are abundant in silica and alumina, to fly ash and kaolin makes them a viable precursor for zeolite synthesis. Recycling discarded porcelain reduces environmental pollution and promotes sustainable material use. This research aims to synthesize Zeolite 13X from waste porcelain insulators through alkali fusion and hydrothermal crystallization, assess the impact of synthesis parameters including NaOH ratio, fusion temperature, and crystallization duration, and characterize the resultant products regarding phase composition, and morphology. The primary objective is to provide an effective, environmentally sustainable method for converting waste porcelain into high-performance Zeolite 13X, appropriate for adsorption and ion-exchange applications.

Materials and Methods

The primary raw material utilized in this investigation was waste porcelain insulator obtained from abandoned high-voltage transmission networks. The porcelain waste was primarily composed of silica (SiO_2) and alumina (Al_2O_3), with trace amounts of quartz and mullite, suggesting it appropriate as an aluminosilicate precursor for zeolite synthesis. Analytical-grade sodium hydroxide (NaOH, ≥98%) and reverse osmosis (RO) water were utilized during the experimental procedure. No foreign sources of silica or alumina were introduced, as the porcelain waste alone supplied adequate reactive oxides for zeolite synthesis.

In this study, the synthesis of Zeolite 13X from porcelain insulator waste via the alkali fusion method was carried out in three main stages: (i) preparation of porcelain waste as the raw material, (ii) alkali fusion and hydrothermal crystallization, and (iii) characterization of the synthesized zeolite. The overall experimental procedure is described as follows.

Raw Materials Preparation

Porcelain insulators waste obtained from decommissioned electrical transmission systems were used as the aluminosilicate precursor for zeolite synthesis. The discarded porcelain was first manually cleaned to remove surface contaminants, metal fittings, and glaze layers, then crushed using a mechanical grinder. The crushed fragments were further pulverized into fine powder using a planetary ball mill to achieve a uniform particle size of approximately 75–100 µm. The resulting porcelain powder was dried at 100 °C for 12 h to eliminate moisture before further processing.

Alkali Fusion Process

The porcelain powder was thoroughly mixed with analytical-grade sodium hydroxide (NaOH pellets) in varying mass ratios of 0.8:1.0, 1.0:1.0, and 1.2:1.0 (NaOH:porcelain insulators waste). The homogeneous mixtures were transferred into alumina crucibles and calcined in an electric muffle furnace at temperatures between 500 °C and 650 °C for 2 h. During this step, NaOH reacted with the aluminosilicate phases (primarily quartz and mullite) to form amorphous sodium aluminosilicate intermediates, which are more reactive during the subsequent hydrothermal process. After fusion, the molten mass was cooled to room temperature and ground into fine fused powder.

Hydrothermal Crystallization

The fused powder was dispersed in deionized water at a solid-to-liquid ratio of approximately 1 : 5 (g:mL) and stirred until complete homogenization. The suspension was then subjected to a two-step crystallization process:

1. Pre-crystallization step: the slurry was aged at different temperatures ranging from room temperature to 70 °C for 2 h;
2. Crystallization step: the aged slurry was transferred to a Teflon-lined stainless-steel autoclave and maintained at 80 °C to 90 °C for 24 h under static conditions.

After hydrothermal treatment, the crystallized solids were filtered, repeatedly washed with deionized water until the pH of the filtrate was neutral, and then oven-dried at 100 °C for 12 h. The dried powders were gently ground to obtain the final Zeolite 13X products.

The samples are known as x:x-TC, where x represents the ratio of NaOH to porcelain insulator waste, and T denotes the fusion temperature in degrees Celsius.

Results and Discussion

The chemical composition of the porcelain insulator waste was analyzed using X-ray fluorescence (XRF) after grinding the sample to a fine powder passing through a 100-mesh sieve (particle size < 150 µm). The quantitative oxide composition is summarized in **Table 1**, The results reveal that the material is primarily composed of silica ($SiO_2 \approx 60.99$ wt%) and alumina ($Al_2O_3 \approx 25.00$ wt%), which are the dominant framework-forming oxides in porcelain ceramics. Minor oxides such as CaO, K_2O, Fe_2O_3, and MgO were also detected, together with trace elements including Ti, Cr, Mn, Na, S, Zn, and Ba. These fluxing and coloring oxides are known to influence the sintering behavior and reactivity of porcelain materials during thermal or alkali activation.

Table 1 Chemical composition of porcelain insulator waste.

Component	wt%
SiO_2	60.99
Al_2O_3	25.00
Fe_2O_3	2.98
MgO	1.14
K_2O	3.16
CaO	4.68
TiO_2	0.54
Cr_2O_3	0.19
MnO	0.14
Na_2O	0.51
SO_3	0.17
ZnO	0.06
BaO	0.12
Others	0.22

The phase composition of the porcelain insulator waste was further examined using X-ray diffraction (XRD), as shown in **Figure 1**. The diffractogram reveals sharp reflections corresponding to quartz (SiO_2), mullite ($3Al_2O_3 \cdot 2SiO_2$), and corundum (Al_2O_3), with minor cristobalite peaks also present. These phases indicate a highly crystalline aluminosilicate framework typical of fired porcelain insulators. Such results are consistent with previous studies reporting quartz and mullite as the major crystalline phases in porcelain and ceramic insulator wastes, which contribute to their mechanical and thermal stability [3]. The coexistence of Si- and Al-rich crystalline phases further supports the suitability of this waste as a precursor for Zeolite 13X synthesis, since these aluminosilicate components can be transformed into sodium aluminosilicate frameworks through the alkali fusion–hydrothermal process.

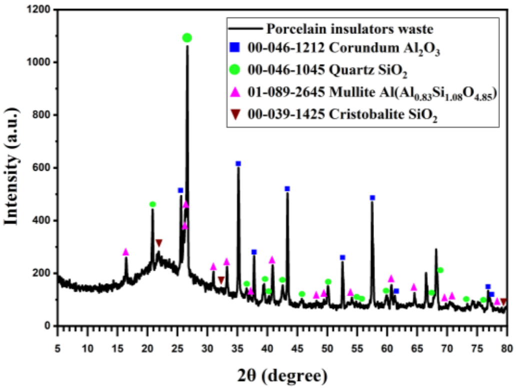

Figure 1 XRD pattern of porcelain insulators waste.

The XRD patterns in **Figure 2(a–b)** illustrate the influence of alkali concentration and fusion temperature on the phase evolution of porcelain insulator waste during the alkali fusion process. As shown in **Figure 2(a)**, increasing the NaOH:porcelain insulators waste ratio from 0.8 to 1.2 at 500 °C led to a gradual reduction in the characteristic peaks of quartz (2θ ≈ 20.8°, 26.6°) and mullite (2θ ≈ 16.4°, 25.9°), accompanied by the emergence and intensification of sodium aluminosilicate ($NaAlSiO_4$) reflections. This trend indicates that a higher alkali concentration enhances the dissolution of Si–O–Al bonds and promotes the formation of reactive sodium aluminosilicate intermediates. The increased presence of Na^+ ions accelerates ion exchange and the breakdown of the original aluminosilicate framework, transforming crystalline quartz and mullite into amorphous or partially crystalline sodium aluminosilicate phases. Such behavior is consistent with previous studies reporting that elevated alkali content significantly improves the conversion efficiency of aluminosilicate sources during zeolite precursor preparation [4,8].

Similarly, **Figure 2(b)** reveals the effect of fusion temperature (500–650 °C) at a fixed

NaOH:porcelain insulators waste ratio of 1.2:1. As the temperature increased, $NaAlSiO_4$ peaks became sharper and more intense, while residual quartz and mullite nearly disappeared at 650 °C, suggesting a complete phase transformation and improved crystallinity. This outcome reflects the crucial role of thermal energy in facilitating the diffusion of Na^+ ions and the reorganization of the Si–Al framework into stable sodium aluminosilicate structures. Comparable results have been reported for the thermal activation of kaolinite- and basalt-derived materials, where higher fusion temperatures promoted homogeneous melting, structural rearrangement, and enhanced crystallinity of sodium aluminosilicate products [4,9]. Overall, the combined influence of high alkali concentration and sufficient thermal activation demonstrates that the optimal fusion condition NaOH:porcelain insulators waste ratio = 1.2:1 and 650 °C produces the most reactive and crystalline precursor, providing a suitable phase composition for subsequent hydrothermal synthesis of FAU-type Zeolite 13X.

As illustrated in **Figure 3(a–b)**, the XRD patterns of the synthesized powders exhibit the characteristic diffraction peaks of zeolite A (NaA) located at $2\theta \approx 7.2°$, 10.1°, 12.4°, 16.1°, 21.7°, 23.9°, 27.1°, and 34.1°, which correspond to the (200), (220), (222), (420), and (511) planes of cubic NaA. These reflections are consistent with standard JCPDS data and previously reported hydrothermal syntheses of NaA from kaolin- and porcelain-derived aluminosilicates [15-17].

At 80 °C in **Figure 3(a)**, the diffraction peaks are sharp and well defined, indicating high crystallinity and phase purity without secondary reflections. This suggests the amorphous aluminosilicate precursors were completely converted into the NaA framework under moderate hydrothermal energy [16,18]. In contrast, the sample crystallized at 90 °C as shown in Figure 1(b) was slightly broadened and asymmetric NaA peaks with additional minor reflections at $2\theta \approx 26°–36°$, corresponding to sodalite or sodium aluminosilicate hydrate [17,19]. These new reflections imply that excessive temperature promotes not only faster nucleation and growth of NaA but also secondary transformation into sodalite, a denser and thermodynamically stable phase [15, 17-20].

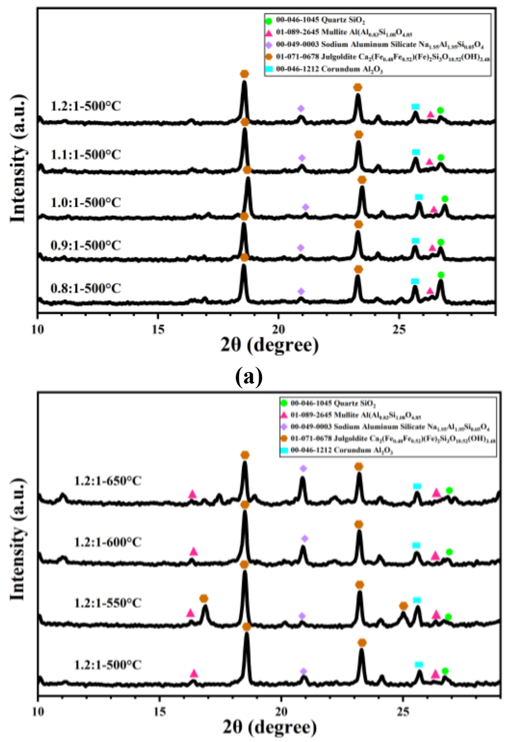

(b)

Figure 2 XRD patterns of **(a)** fused powder prepared at 500 °C with varying NaOH/porcelain ratios (0.8–1.2/1), **(b)** fused powder prepared at different temperatures (550–650 °C) for the 1.2:1 of NaOH/porcelain ratio, crystallization at 90 °C for 24 h. at 2θ =10-30 degree

Such phase transformation (NaA to sodalite) with increasing temperature aligns with the Ostwald ripening sequence reported by *Liu et al.* (*Powder Technol.* 243, 184–193, 2013) and other studies on waste to zeolite 13X and NaA [14, 12-13,20]. Temperatures above 90 °C or prolonged reaction times (> 6 h) accelerate condensation of Si–O–Al linkages, reducing NaA selectivity [14, 11-12,20].

In summary, the XRD comparison confirms that 80 °C yields optimal crystallization of pure zeolite A, while 90 °C promotes partial conversion toward sodalite, decreasing phase purity and relative crystallinity [10, 14 18,20].

The SEM micrographs shown in **Figure 4(a–f)** clearly depict morphological evolution of the fused and crystallized products during the alkali fusion hydrothermal process. At low NaOH:porcelain insulators waste ratio (0.8–0.9 : 1), irregular dense agglomerates without distinct crystal boundaries were observed, indicating incomplete decomposition of quartz and mullite phases. Increasing the NaOH:porcelain insulators waste ratio to 1.2 : 1 and raising the fusion temperature to 650 °C produced porous and angular particles, suggesting the formation of reactive sodium–aluminosilicate precursors suitable for zeolite crystallization. After hydrothermal treatment, the

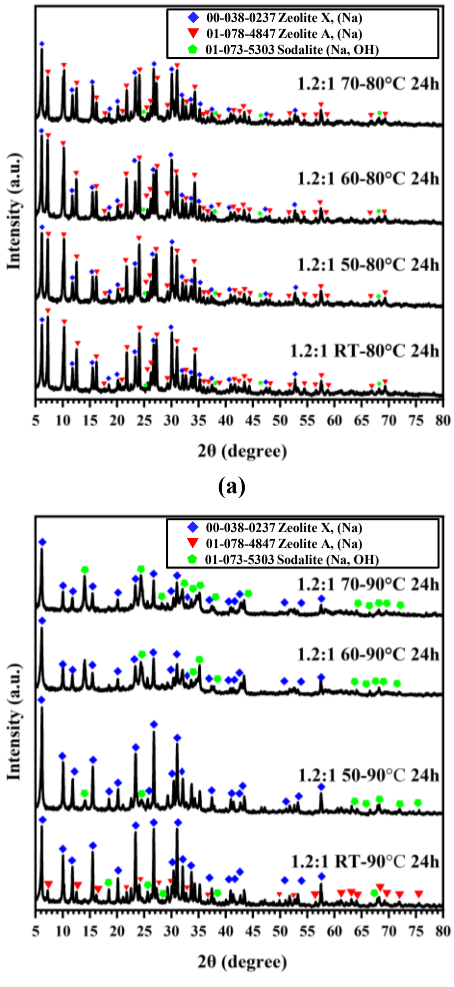

(a)

(b)

Figure 3 XRD patterns of samples after pre-crystallization at RT to 70 °C and crystallization at **(a)** 80 °C and **(b)** 90 °C for 24 h.

average particle sizes were 1.12, 1.46, and 0.81 µm for 50–90, 70–80, and 70–90 °C conditions, respectively. Notably, the sample prepared at 70–80 °C showed uniform cubic morphology with sharp edges, characteristic of zeolite A (NaA) [14], while higher-temperature synthesis led to smaller, irregular particles and partial agglomeration, implying secondary nucleation or phase transformation toward sodalite. These results confirm that moderate hydrothermal conditions favor nucleation and growth of cubic zeolite A crystals, whereas excessive temperature promotes amorphous or transitional phases.

Conclusion

In this study, zeolite 13X was successfully synthesized from discarded porcelain insulator waste via the alkali fusion–hydrothermal method without the addition of external silica or alumina sources. The porcelain waste, primarily composed of SiO_2 and Al_2O_3, proved to be an effective aluminosilicate precursor for zeolite formation. The synthesis parameters, including the NaOH-to-waste ratio and fusion temperature, significantly affected the dissolution of quartz and mullite, as well as the crystallinity of the resulting zeolite. The optimal conditions were identified at a NaOH:porcelain waste ratio of 1.2:1 and a fusion temperature of 650 °C, which facilitated complete phase transformation to reactive sodium aluminosilicate intermediates. Subsequent hydrothermal crystallization at 80 °C for 24 h yielded highly crystalline zeolite A (NaA) with uniform cubic morphology, while crystallization at 90 °C induced partial conversion to sodalite. These findings demonstrate that precise control of alkalinity and temperature is critical for obtaining phase-pure FAU-type zeolite 13X. Furthermore, the

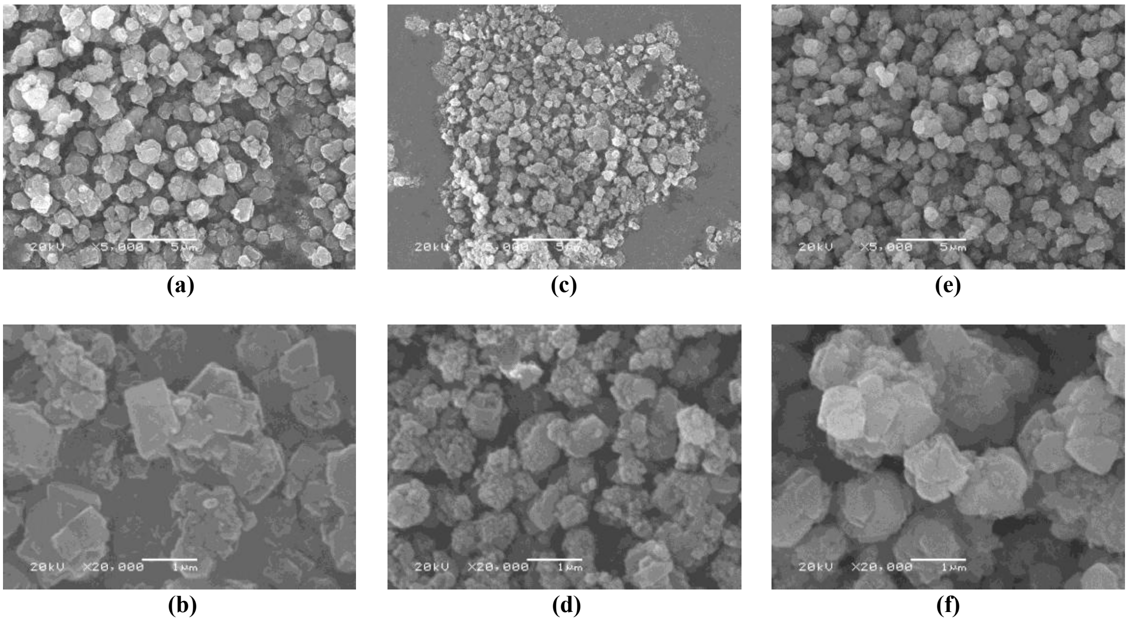

(a) (c) (e)

(b) (d) (f)

Figure 4 SEM micrographs of samples after pre-crystallization at 70 °C and crystallization at **(a–b)** 80 °C, **(c–d)** 90 °C and after pre-crystallization at 50 °C and crystallization at 90 °C **(e-f)** for 24 h.

results confirm that porcelain insulator waste can serve as a sustainable and low-cost raw material for zeolite 13X synthesis, aligning with circular economy principles and offering a promising route for CO_2 adsorption and environmental remediation applications.

Acknowledgements

The author gratefully acknowledges the Upcycled Materials from Industrial and Agricultural Wastes Research Unit, Department of Materials Science, Faculty of Science, Chulalongkorn University for supporting this research.

References

1. P. Janys, R. Prochazka, The behaviour of insulator strings under dry and wet conditions, *Proc. 17th Int. Sci. Conf. on Electric Power Engineering (EPE)*, 16–18 May (2016).
2. M. Ocampo, A. González, Ceramic waste reuse and valorization alternatives: A review, *Rev. EIA*, **20**, (2023).
3. T. Wajima, Y. Ikegami, Synthesis of zeolitic materials from waste porcelain at low temperature via a two-step alkali conversion, *Ceram. Int.*, **33**(7), 1269–1274 (2007).
4. T. Abdullahi, Z. Harun, M. H. D. Othman, A review on sustainable synthesis of zeolite from kaolinite resources via hydrothermal process, *Adv. Powder Technol.*, **28**(8), 1827–1840 (2017).
5. T. Wajima, H. Sugawara, Y. Ikegami, Effect of pre-aging and hydrothermal conditions on morphology and crystallinity of Zeolite X synthesized from waste materials, *J. Asian Ceram. Soc.*, **8**, 459–466 (2020).
6. A. Chen, L. Teng, R. Li, X. Liu, Crystallization mechanism of zeolite A from coal kaolin, *Microporous Mesoporous Mater.*, **176**, 71–78 (2013).
7. M. Yousaf, M. A. Rafiq, A. S. Khan, M. N. Khan, Microstructural and mechanical characterization of high strength porcelain insulators for power transmission and distribution applications, *Ceram. Int.*, **48**(2), 1603–1610 (2022).
8. F. Su, C. Lu, CO_2 capture from gas stream by zeolite 13X using a dual-column temperature/vacuum swing adsorption, *Energy Environ. Sci.*, **5**(10), 9021–9027 (2012).
9. G. Ke, H. Shen, P. Yang, Synthesis of X-zeolite from waste basalt powder and its influencing factors and synthesis mechanism, *Materials*, **12**(23), 3895 (2019).
10. A. Chen, C. Wang, Reaction kinetics regulated formation of short-range order in an amorphous matrix during zeolite crystallization, *Chem. Eng. J.*, **426**, 131520 (2021).
11. F. Su, C. Lu, CO_2 adsorption enhancement on NaX zeolite by improved pore accessibility and crystallinity, *Microporous Mesoporous Mater.*, **156**, 90–97 (2012).
12. T. Wajima, K. Yoshizuka, T. Hirai, Y. Ikegami, Synthesis of zeolite X from waste sandstone cake using alkali fusion method, *Mater. Trans.*, **49**(3), 612–618 (2008).
13. S. Gao, Y. Li, X. Zhao, Y. Wang, H. Liu, Synthesis of zeolites from low-cost feeds and its sustainable environmental applications, *J. Environ. Chem. Eng.*, **11**(1), 108995 (2023).
14. Z. Liu, M. Wu, S. Wang, Effect of synthesis parameters on NaA zeolite crystals, *Powder Technol.*, **246**, 520–529 (2013).
15. Z. Zhang, W. Zhang, X. Chen, Q. Xia, Z. Li, Adsorption of CO_2 on zeolite 13X and activated carbon with higher surface area, *Sep. Sci. Technol.*, **45**(5), 710–719 (2010).
16. Z. Zhang, X. Chen, Q. Xia, Z. Li, Adsorption of CO_2 on Zeolite 13X and activated carbon with higher surface area, *Sep. Sci. Technol.*, **45**, 710–719 (2010).
17. Z. Liu, M. Wu, S. Wang, Influence of synthesis parameters on NaA zeolite crystals, *Powder Technol.*, **246**, 520–529 (2013)
18. M. Ulfa, A. Masykur, A.F. Nofitasari, D. Cahyana, A. Ghofur, Synthesis of Zeolites from Coal Fly Ash Using Alkaline Fusion and Its Applications in Removing Heavy Metals, *Materials*, **16**, 4837 (2023).
19. S. Gao, Y. Li, X. Zhao, Y. Wang, H. Liu, Synthesis of zeolites from low-cost feeds and its sustainable environmental applications, *J. Environ. Chem. Eng.*, **11**, 108995 (2023).
20. J. Li, W. Chen, Effect of synthesis conditions on the properties of 13X zeolites, *Mater. Chem. Phys.*, **261**, 124169 (2021).

Author Index